Histol Histopathol (2024) 39: 671-690

Histology and Histopathology
From Cell Biology to Tissue Engineering

REVIEW Open Access

Histopathological evaluation of infertility: Lessons from laboratory rodents

Albert Markus Ricken[1], Moses Agbomhere Hamed[2,3,4] and Roland Eghoghosoa Akhigbe[4,5]

[1]Institute of Anatomy, Faculty of Medicine, University of Leipzig, Leipzig, Germany, [2]Department of Medical Laboratory Science, Afe Babalola University, Ado-Ekiti, Ekiti State, [3]The Brainwill Laboratory, [4]Reproductive Biology and Toxicology Research Laboratory, Oasis of Grace Hospital, Osogbo, Osun State and [5]Department of Physiology, Ladoke Akintola University of Technology, Ogbomoso, Oyo State, Nigeria

Summary. Infertility is a growing challenge globally with emerging risk factors. There are effective laboratory tests to evaluate infertility in humans, nevertheless, some measures, especially histopathological evaluations, are invasive due to the pain inflicted when accessing the reproductive organs and obtaining samples; hence, their relevance may be limited in humans. However, these histopathological evaluations provide essential information on the etiopathogenesis of infertility and the likely mechanisms of action of potential therapeutic candidates. Also, non-invasive methods are available, such as the assay of testosterone in the blood and semen analysis, both of which are predictors of testicular functions. This review provides detailed information on the available histopathological investigations of infertility, such as qualitative and quantitative histopathological assessments of gonadal tissues, specific cell counts, and sperm morphology characterization, with a focus on the procedures, interpretation, and pathophysiological basis. Data from the literature revealed that histopathological examinations of the reproductive organs, as well as spermatozoa, are useful in understanding the pathogenesis of incident infertility. Histopathological evaluation may range from basic hematoxylin and eosin stains to some special stains. Also, histopathological findings (such as spermatogenic cells and planimetric variables, like seminiferous tubule diameter and theca cell and corpus luteum thickness) may be quantified and analyzed for comparison. Some skill is required for these investigations, which may be a limiting factor; however, they are important tools in translational medicine.

Corresponding Author: Roland Eghoghosoa Akhigbe, Department of Physiology, Ladoke Akintola University of Technology, Ogbomoso, Oyo State, Nigeria. e-mail: akhigberoland@gmail.com or reakhigbe@lautech.edu.ng

www.hh.um.es. DOI: 10.14670/HH-18-684

Key words: Folliculogenesis, Infertility, Oocyte, Reproduction, Sperm, Steroidogenesis

Introduction

Infertility, which is defined as the inability of a couple to achieve conception within a year of adequate sexual intercourse (Akhigbe et al., 2022a), is a growing concern as global trends over the last five decades have demonstrated a decline in fertility (Levine et al., 2017; Segal and Giudice, 2022). This has led to more studies in the field of reproductive health and fertility in an attempt to investigate new risk factors (and associated mechanisms) of infertility. Data from animal models should be translated to humans with caution, however, animal models remain a useful tool in translational studies (Khati et al., 2022) due to their attendant merits, such as the availability of homogenous experimental subjects, easy handling of subjects, controlled experimental conditions, and ample tissue sampling (Ajayi and Akhigbe, 2020a).

For fertility assessment, hysterosalpingography, pelvic/abdominopelvic scans, and blood samples for hormone profiles with or without a lipid profile are requested to assess female fertility, while a spermiogram and blood sample for hormone profiles are requested to assess male fertility. Although these investigations lead to an effective assessment of infertility, some histopathological examinations may provide useful additional details. Despite the usefulness of these histopathological assessments, the major drawback is their invasive nature in humans. However, in animal models, these assessments help understand the etiopathogenesis of infertility. The present study reviews available histopathological examinations in the study of reproductive functions in animal models. This provides essential tools from experimental studies to illuminate the etiopathogenesis of emerging risk factors in reproductive dysfunction. Also, this opens up an

opportunity to evaluate potential drug candidates.

The anatomy of the gonads

Description of the testis and epididymis: gross anatomy and histology

Shortly before full term, the testis in humans leaves the outer ring of the inguinal canal and comes to lie permanently in the scrotum (Barteczko and Jacob, 2000). At the same time, the vaginal process loses its direct connection to the abdominal cavity and becomes the tunica vaginalis due to closure of the inguinal canal. In rodents, the testes are located on either side of the urinary bladder. They temporarily shift to the scrotum only during sexual arousal, thereby crossing the inguinal canal, which remains open for life in rodents (Brower, 2018). Dorsally, the testis in humans and rodents is structurally connected to the epididymis at its upper pole and merges into the mesorchium. At its lower pole, the testis has retaining ligaments derived from the gubernaculum testis. These ligaments may play an active role in the temporal displacement of the testis in adult rodents (Lie and Hutson, 2011).

Macroscopy of the adult epididymis in humans and rodents is almost identical. Although the epididymis is a highly tortuous single duct, it is subdivided into caput, corpus, and cauda from the testis to the seminal duct (Merkwitz et al., 2016b). In both humans and rodents, blind-ending diverticula are found as derivates of the paramesonephric duct (appendix testis) and the mesonephric duct (appendix epididymis) in the testicular and epididymal regions, respectively (Del Vecchio, 1981).

The histology of the testis is presented in Figure 1. The adult testis in humans and rodents has a uniform structure. Connective tissue septa extend from the tunica albuginea to the testicular hilus and divide the testis into longitudinal lobules. Within each testicular lobule lie several testicular tubules, beginning and ending with two straight sections (tubuli recti) at the hilus and extending to the tunica albuginea with a tortuous, closed section (tubulus contortus). The tubuli recti provide the connection to the rete testis, followed by the ductuli efferentes at the testicular hilus. The tubuli recti are lined by a single-layered cubic epithelium. The tubulus contortus has an age-dependent central lumen and is lined with the germinal epithelium. This consists of a different number of layers and different stages of spermatogenesis, depending on age and, in some rodents, season; in humans, six manifestations in the germ cell cycle are distinguished, and in rodents, many more (Khati et al., 2018).

The seminiferous epithelium is divided into basal and adluminal (apical) sections by the blood-testis barrier, which is also referred to as the Sertoli cell epithelial barrier formed by specific coexisting actin-based tight junctions, basal ectoplasmic specialization, gap junctions, and intermediate filament-based desmosomes (Pelletier et al., 2011; França et al., 2012). At the periphery of the seminiferous tubules are the spermatogonia, which are located inside the basement membrane. Above the spermatogonia, towards the center, the germ cells are in mitosis, meiosis, and differentiation into spermatozoa. The migration and transformation of germ cells from the basal to the central takes about 70 days in humans, 35 days in mice, and 50 days in rats (Perrard et al., 2016; Ajayi and Akhigbe, 2020b). The accessory Sertoli cells extend vertically from the basement membrane to the tubule center. The Sertoli cells are interconnected by close cell-cell contacts. This forms an effective blood-testis barrier between the peripheral abluminal compartment, which contains primordial germ cells, germ cells in mitosis, and initiated meiosis, and the central adluminal compartment, which contains germ cells in advanced meiosis and differentiating into spermatozoa (Mruk and Cheng, 2015). Between the testicular tubules are the other testicular accessory cells, the eosinophilic Leydig cells, with a large, round nucleus, a dispersed karyoplasm, and a distinct nucleolus. So-called Reineke crystals are observed in Leydig cells in humans and some rodents (Kerr et al., 1986; Planinić et al., 2022). In seasonally breeding rodents, spermatogenesis is largely discontinued during the non-breeding period, and only spermatogonia and germ cells in the early stages of meiosis are found in the seminiferous tubules (Khati and Hammouche, 2021).

Besides spermatogenesis, the key function of the testis is to synthesize testosterone, which is influenced by the hypothalamic-pituitary-testicular axis, through the action of luteinizing hormone (LH) on the Leydig cells (Ajayi and Akhigbe, 2020c; Oyedokun et al., 2023). Spermatogenesis, which is influenced by the action of follicle-stimulating cells on the Sertoli cells, is additionally maintained by optimal levels of intratestinal levels of testosterone (Ajayi and Akhigbe, 2020c; Oyedokun et al., 2023). Spermiogenesis in the seminiferous tubules takes about 22.7 days in rats and 21.6 days in humans (Suarez, 2002; Zirkin and Goldberg, 2018). It involves acrosome formation, which is crucial for penetration into the zona pellucida of the Oocyte and, thus, for fertilization. After spermiogenesis, the spermatozoa are morphologically mature, however, they are non-motile and incapable of fertilizing an egg. Spermatozoa are passively moved from the seminiferous tubules to the caput of the epididymis by testicular fluid passing through the rete testis and efferent ductules. The fluid pressure produced in the seminiferous tubules, the contraction of the smooth muscles, and the ciliary currents in the efferent ductules all help facilitate this transition. The spermatozoa remain in the extremely convoluted duct of the epididymis for around 12 days, where they undergo biochemical maturation related to the alteration of glycoproteins in the sperm head's plasma membrane. When the spermatozoa get to the caudal epididymis, they are fully mature and motile, capable of fertilizing an egg. Hence, the epididymides

play a significant role in male fertility.

Description of the ovary and uterus: gross anatomy and histology

In humans, the adult ovaries are located intraperitoneally on the dorsal side of the broad ligament at the junction of the greater and lesser pelvis. In contrast, the ovaries in rodents remain near the former primordium and are located on the posterior wall of the abdominal cavity, lateral to the lower half of the kidney (Kaufman, 2010). Except where the mesovarium enters the ovary in rodents, it is surrounded by a transparent bursa.

The uterus, fallopian tubes, and parts of the vagina develop from the two paramesonephric ducts in humans and rodents (Cunha et al., 2019). The two ducts unite centrally but to different degrees in humans and rodents. In humans, they largely fuse to form the uterus and the proximal portion of the vagina. In contrast, in rodents, they fuse only in their distal parts to form the cervix uteri and vagina. The proximal parts remain separate and form the two uterine horns in addition to the fallopian tubes. In rodents, the two uterine horns are suspended from the posterior wall of the abdominal cavity by broad mesenteries (Rendi et al., 2012). In humans, the pear-shaped uterus lies with the fundus and corpus intraperitoneally, the cervix uteri is firmly anchored to its endocervix by retaining ligaments in the lesser pelvis (Ferenczy, 1977). The uterus with its exocervix protrudes a good distance into the vagina and forms an anterior and posterior fornix in addition to lateral fornices, which are also found in rodents (Carretero et al., 2017). In both humans and rodents, epoophorons are

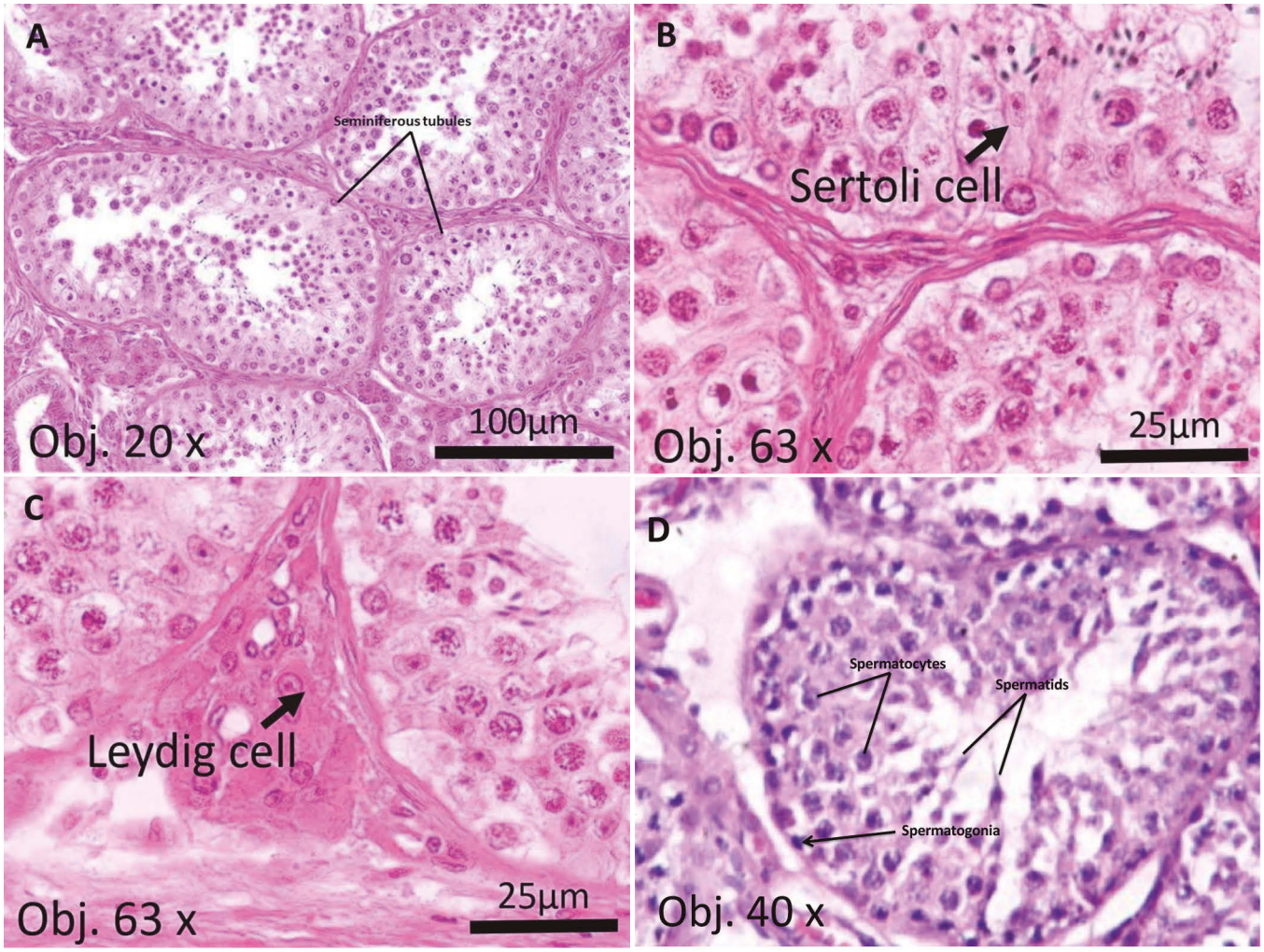

Fig. 1. Histology of the human testis showing the seminiferous tubules **(A)**, Sertoli cell **(B)**, and Leydig cell **(C)**, and that of the testis of a rabbit **(D)** showing the spermatogenic cells (spermatogonia, spermatocytes, and spermatids). Fig. 1A-C are unpublished photomicrographs from our laboratory (Institute of Anatomy, Faculty of Medicine, University of Leipzig, Leipzig, Germany), while 1D is also from our laboratory (Reproductive Biology and Toxicology Research Laboratory, Oasis of Grace Hospital, Osogbo, Osun State, Nigeria) but has been published (Akhigbe and Ajayi, 2020).

found as derivates of the paramesonephric duct in the region of the ovarian hilus (Jia and Zhao, 2022). Whether rodents, like humans, can form a Gartner duct has not yet been conclusively investigated.

The histology of the ovary and uterus are presented in Figure 2. The adult ovary of humans and rodents can

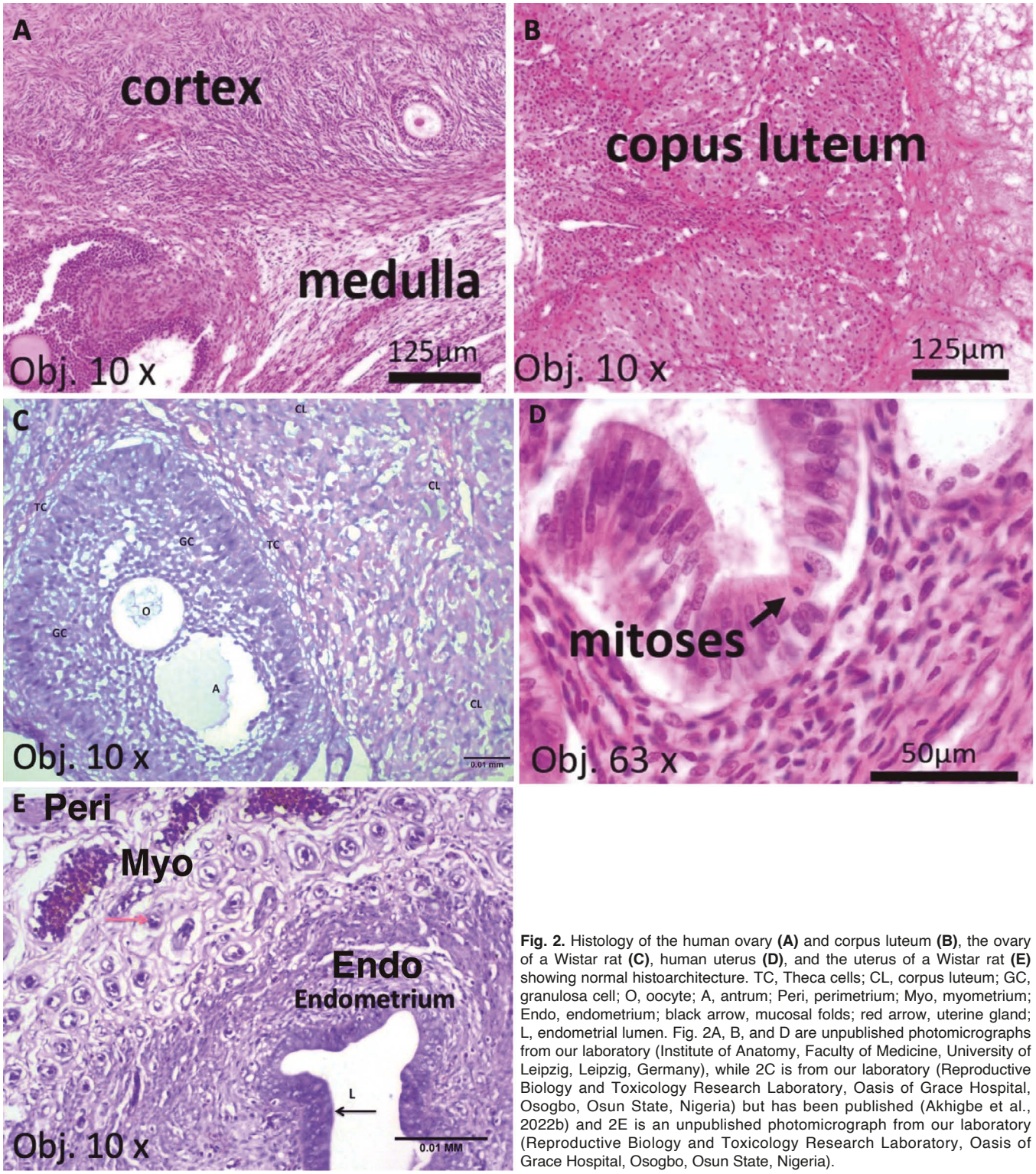

Fig. 2. Histology of the human ovary **(A)** and corpus luteum **(B)**, the ovary of a Wistar rat **(C)**, human uterus **(D)**, and the uterus of a Wistar rat **(E)** showing normal histoarchitecture. TC, Theca cells; CL, corpus luteum; GC, granulosa cell; O, oocyte; A, antrum; Peri, perimetrium; Myo, myometrium; Endo, endometrium; black arrow, mucosal folds; red arrow, uterine gland; L, endometrial lumen. Fig. 2A, B, and D are unpublished photomicrographs from our laboratory (Institute of Anatomy, Faculty of Medicine, University of Leipzig, Leipzig, Germany), while 2C is from our laboratory (Reproductive Biology and Toxicology Research Laboratory, Oasis of Grace Hospital, Osogbo, Osun State, Nigeria) but has been published (Akhigbe et al., 2022b) and 2E is an unpublished photomicrograph from our laboratory (Reproductive Biology and Toxicology Research Laboratory, Oasis of Grace Hospital, Osogbo, Osun State, Nigeria).

be divided into an epithelium-covered cortex of cell-rich, fibrous, spinocellular connective tissue, a central, well-vascularized medulla, and a hilar region. Two types of ovarian follicles can be distinguished; those that lie directly beneath the surface epithelium in conspicuously avascular areas and form the reserve pool of ovarian follicles (primordial follicles), and those that have entered folliculogenesis and grow and mature in a well-orchestrated manner over several ovarian cycles. During folliculogenesis, follicles shift temporarily from the areas of low vascularity to the more vascularized areas of the ovary (Martelli et al., 2017). Although most primordial follicles in rodents contain only one oocyte, as in humans, follicles containing two oocytes are not uncommon in rodents. The follicles in folliculogenesis in humans and rodents can be divided essentially into those without an antrum and those with an antrum. The granulosa cells in the antral follicles can be subdivided at least into basal, antral, and cumulus oophorus granulosa cells according to function and occurrence, whereas this subdivision differs in humans and rodents. Of the follicles selected for final maturation within an ovarian cycle, usually only one makes it to ovulation in humans, and several in rodents (Chaffin and VandeVoort, 2013). The other subdominant follicles become atretic. After the oocyte leaves the ovulated follicle with its surrounding granulosa cells, the corpus luteum is formed from the remaining follicular wall. At the end of an ovarian cycle without pregnancy, the corpus luteum undergoes connective tissue remodeling over several cycles in humans and rodents, forming a nonfunctional corpus albicans in humans (Morales et al., 2000; Sato et al., 2014). The initially basophilic and then eosinophilic corpora lutea in rodents degrades over 2-4 more cycles if pregnancy does not occur.

In all uterine segments in humans, the endometrium is covered luminally by a single-layered, highly columnar epithelium from which unbranched glands descend into the lamina propria of reticular connective tissue (Ferenczy, 1977; Ferenczy and Wright, 2013). In the endocervix, the glands are mucinous differentiated. The lamina propria below the epithelium is more fibrous here than in the fundus/corpus area. The uterine horns of rodents have mucosa lying in the transverse folds, which are lined by a single-layered columnar epithelium. Branching glands extend from the epithelium into the lamina propria (Steward et al., 2011; Vu et al., 2018). In some rodents, the glands can even extend into the myometrium. In contrast to humans, the entire mucosa of the cervix in rodents is covered by a multilayered squamous epithelium from which no glands extend. The tunica muscularis is more clearly divided into an inner circular and an outer longitudinal layer in rodents than in humans and has increasingly collagenous connective tissue toward the cervix.

In humans, the endometrium in the fundus/corpus area of the uterus builds up and breaks down cyclically in three phases under the influence of ovarian hormones. After the menstrual phase, a new receptive stratum functionalis develops from the stratum basalis in the proliferative and secretory phase. Menstrual bleeding comparable to that in humans does not normally occur in rodents; instead, the endometrium is cyclically reabsorbed. The only exception described so far is the spiny mouse (Bellofiore et al., 2017). The reason for the absence of menstrual bleeding in rodents could be that the decidualization of the endometrium begins only after implantation. In rodents, even the cyclic changes of the vaginal mucosa are more evident than those of the endometrium. Based on the histology of the vaginal mucosa, the actual cycle phase can be accurately determined (Merkwitz et al., 2016a).

In humans, the female reproductive cycle is referred to as the menstrual cycle, which includes ovarian and uterine cycles and lasts an average of 28±7 days, whereas in rodents, it is referred to as the estrus cycle that includes proestrus, estrus, metestrus, and diestrus and lasts about 4 to 5 days (Ajayi and Akhigbe, 2020a). The ovaries contain the follicles that are transformed from the primordial follicle to the primary, secondary, and tertiary follicles with a large antrum, which is referred to as the Graafian follicle. The primordial follicles have one layer of squamous follicular cells and are located under the cortex, whereas primary follicles are lined by a layer of cuboidal follicular cells and secondary follicles are lined by several layers of cuboidal granulosa cells without an antrum/antral space (Akhigbe et al., 2022b). Follicles with multiple layers of cuboidal granulosa cells, just like secondary follicles, but with a fluid-filled cavity forming, are called early antral follicles (tertiary follicles), while follicles with a large antrum and a prominent cumulus oophorus are called Graafian (pre-ovulatory) follicles (Akhigbe et al., 2022b). The production of fertilizable eggs in folliculogenesis, like spermatogenesis in the testis, is the main goal of the ovary; another, no less important, goal is the production of estrogen in the maturing follicles and progesterone in the corpora lutea to prepare the endometrium for conception.

Histopathological assessment of male fertility

Gonadal tissue processing for histopathological evaluation

The gonads, which consist of testes and ovaries, are charged with two main tasks, namely gametogenesis and synthesis of sex steroid hormones (Nussey and Whitehead, 2001). Since the process of autolysis begins immediately after cell death (Arnold, 2018), it is important to fix samples as quickly and thoroughly as possible after sampling (Slaoui et al., 2017). Because prognosis and treatment strategies for several gynecological diseases and reproductive biology problems depend on accurate tissue diagnosis, appropriate postmortem tissue preservation, and

processing prior to analysis are necessary to preserve cellular features and conserve antigens and nucleic acid sequences (Comanescu et al., 2012). Only with adequate tissue preservation is it possible to assess whether the observed changes are artificial, natural, or pathological (Slaoui et al., 2017). In light of this, it is crucial that each step of tissue preservation and examination is strictly standardized (i.e., specimen sampling, trimming, embedding, sectioning, and staining) (Slaoui et al., 2017).

To achieve effective tissue preservation, tissue samples must be immersed in a ten-fold volume of fixative. The fixation technique most commonly used in biomedical research involves immersing the tissue samples in four to ten percent buffered formaldehyde or paraformaldehyde (Slaoui et al., 2017). Following fixation, tissue samples are trimmed to the correct size, orientated, and placed in an embedding cassette (Morawietz et al., 2004). This is followed by a step-by-step process in which the tissue samples are dehydrated in a graded ethanol series, cleared with xylene, and infiltrated with paraffin (Patil, et al., 2015; Slaoui et al., 2017). After the paraffin has penetrated the tissue samples, the samples are removed from the embedding cassettes and carefully placed in base molds into which paraffin is poured. The molds are then placed on a cooling surface (Slaoui et al., 2017). For sectioning, the paraffin blocks with the tissue samples are placed in sample holders of a sled or rotary microtome (Slaoui and Fiette, 2011). From the tissue samples, three to ten-µm thick sections are cut into ribbons and stretched by floating on a water bath at 45°C (Slaoui and Fiette, 2011; Soukup and Tylová, 2014; Stasolla and Yeung, 2015). Since they are too low in contrast to be evaluated in their present state, they are stained or subjected to immunohistochemical analysis for particular cell antigens (Slaoui et al., 2017). The routine stain for histopathological alterations in tissues and organs is hematoxylin and eosin (H&E) (Slaoui and Fiette, 2011; Bolon, et al., 2021). After H&E staining, the sections are covered with a thin coverslip glass to preserve them and improve their visual assessment with a light microscope (Slaoui et al., 2017; Goacher et al., 2017).

Sometimes, some special stains can be useful to identify specific lesions. Trichome staining, which uses two or more acid dyes in combination with a polyacid, helps to identify an increase in collagenous fibers, which is typical of fibrotic changes (Baker, 1958). Pearls' Prussian blue is important for the detection of iron in tissues or cells. In this technique, no dye is applied; instead, the tissue is treated with hydrochloric acid, whereby the iron deposited therein reacts with potassium ferrocyanide to form iron (III) ferrocyanide, an insoluble light-blue pigment (Ghio and Roggli, 2021). Verhoeff's stain (or Verhoeff-Van Gieson stain) demonstrates pathologic elastic fibers (Puchtler and Waldrop, 1979). Periodic acid Schiff's (PAS) helps demonstrate glycogen accumulation in tissues and cells (Sheehan and Hrapchak, 1973).

Histopathological evaluation of the testis and epididymis

The testes and epididymides may be examined for tissue damage, spermatogenesis, and cell counts.

Qualitative report

Usually, histological sections of the testis are examined under a light microscope at 100x magnification (Obj. 10x) to obtain a comprehensive overview, and at 400x magnification (Obj. 40x) to identify specific lesions and to take photomicrographs. Lesions observed may not necessarily be pathognomonic for a specific harmful exposure, however, they do depict testicular toxicity (Akhigbe and Ajayi, 2020).

Figure 3 shows testicular photomicrographs of different lesions, ranging from vascular congestions, widened interstitial space, shrunken seminiferous tubules, desquamation of the tunica propria, detachment and degeneration of spermatogenic cells, cell maturation arrest, degeneration of seminiferous tubules, and spermatogenic cells. These anomalies have been reported with the use of medications, such as highly active antiretroviral medications, anti-tuberculosis medications, codeine, and Rohypnol (Akhigbe et al., 2021a, 2023; Ajayi et al., 2023; Hamed et al., 2023).

Experimental studies in animal models have shown that diabetes leads to shrinkage of seminiferous tubules, widening of the interstitial space, and degeneration of spermatogenic cells (Babaei et al., 2021; He et al., 2021). Experimentally induced obesity (Mu et al., 2017) and exposure to heavy metals such as lead (Besong et al., 2023a), cadmium (Ige et al., 2012a), and aluminum (Ige et al., 2012b) have also been shown to cause seminiferous tubule shrinkage, spermatogenic cell degeneration, and sperm reduction in the tubule lumen.

Similarly, lesions observed in the epididymides are usually not pathognomonic of a specific adverse event. Figure 4A shows a normal human epididymis with normal intertubular space and tubules in which the lumen contains sufficient/normal spermatozoa. Anomalies in the epididymis range from widening of the intertubular space to widening of the tubular lumen and reduced or absent spermatozoa. There may also be desquamation of the tubular membrane.

Cosentino's score

Testicular histology can be assessed for testicular damage using Cosentino's scoring system.

According to this system, testes are divided into four grades depending on the preservation of the testicular histoarchitecture (Cosentino et al., 1985; Akhigbe et al., 2021a; Afolabi et al., 2022a). Grade 1 denotes normal testicular histoarchitecture, whereas grade 4 denotes a damaged testis with coagulative necrosis of the seminiferous tubules (Table 1). It is important that each tissue section is scored by two experts blinded to the study protocol and that the mean value of their scores is used.

Table 1. Cosentino's grading for testicular histoarchitecture.

Grade	Features observed
1	Normal testicular tissue with an orderly arrangement of germ cells
2	Loss of cohesion in germ cells, closely packed seminiferous tubules
3	Disordered and sloughed germ cells with shrunken and pyknotic nuclei, impaired borders of the seminiferous tubules
4	Irregular and damaged seminiferous tubules filled by coag- ulative necrosis in the germ cells

Cosentino et al., 1985; Akhigbe et al., 2021a; Afolabi et al., 2022a.

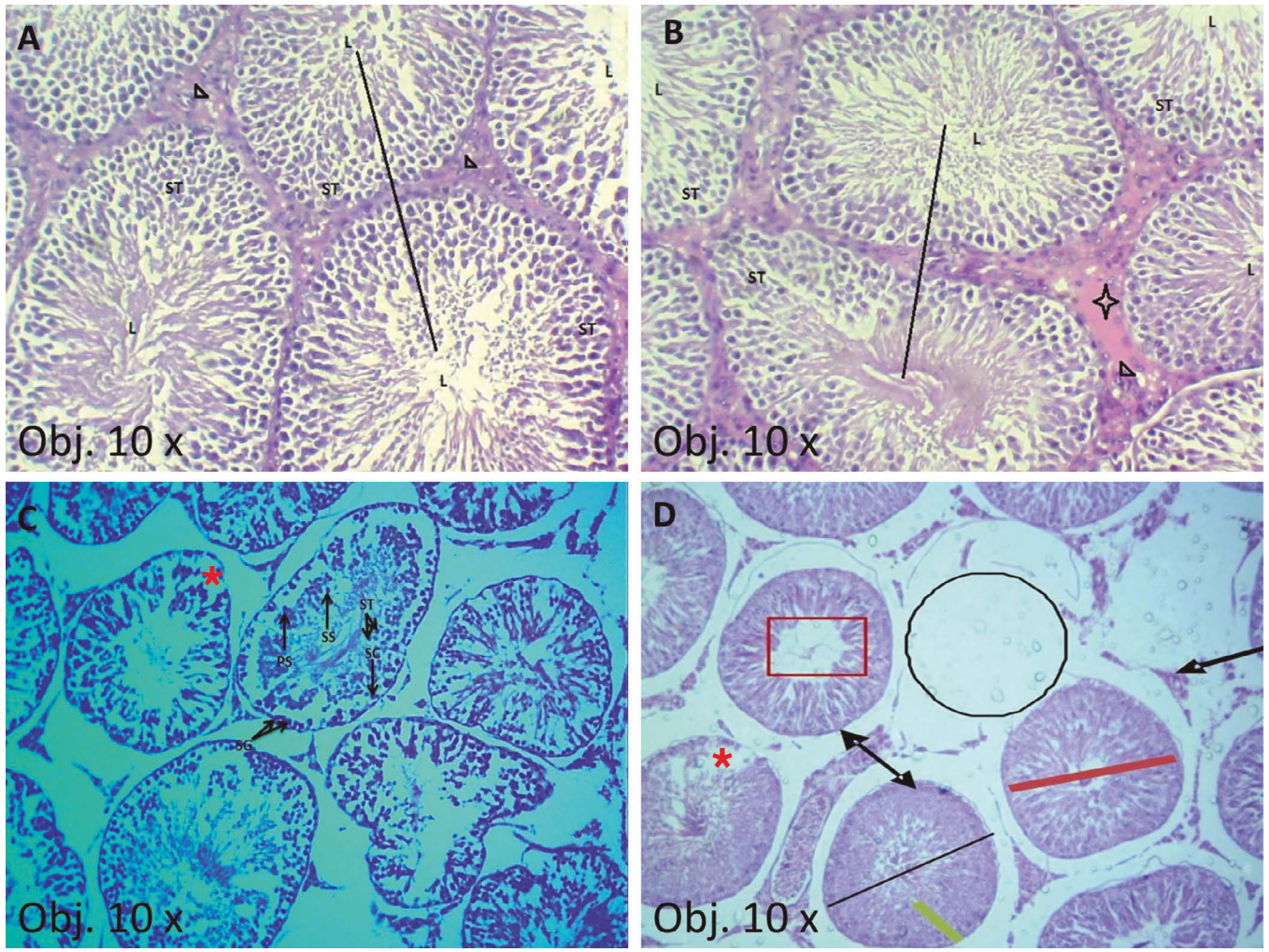

Fig. 3. Histology of the testis of the rat showing preserved histoarchitecture with normal seminiferous tubules (ST) with germ cells at varying degree of maturation (span), the lumen (L) containing adequate sperm cells, and the interstitial space appears normal with normal Leydig cells (arrow head) **(A)**. There is a focal vascular congestion (star) in the interstitial space in **(B)**. **C.** Shows desquamated basement membrane of the seminiferous tubules (black arrow), widened interstitial space (arrow with double head), and degenerated spermatogenic cells (red asterisk). The interstitial space is widened (arrow with double head) withsoma Leydig cells (black arrow) appearin normal. Some tubules show germ cells varying degree of maturation (red bar). **D.** Shows seminiferous tubules with scanty sperm cells in the tubular lumen (red box), and degeneration of the seminiferous tubule (black circle) and spermatogenic cells (red asterisk). SG, Spermatogonia; SC, Sertoli cell; PS, primary spermatocyte; SS, secondary spermatocyte; ST, spermatid. Photomicrographs are from our laboratory (Reproductive Biology and Toxicology Research Laboratory, Oasis of Grace Hospital, Osogbo, Osun State, Nigeria) and have been published, Fig. 3A and B (Akhigbe et al., 2021a), Fig. 3C (Akhigbe et al., 2023), Fig. 3D (Ajayi et al., 2023; Hamed et al., 2023).

Planimetry

This involves the measurement of different testicular and epididymal tissue areas (Fig. 4). A ruler adapted to the microscope can be used for this purpose. In addition, captured photomicrographs can be uploaded to Image J, which is equipped with specific plugins for measuring these areas. Usually, seminiferous tubular diameter, epithelial height, and seminiferous luminal diameter are measured. Epithelial height is measured in four different areas and the mean is calculated. The diameters of the seminiferous tubule and lumen are obtained by measuring the major and minor axes and then calculating the mean. A reduced seminiferous tubular diameter indicates shrinkage of the seminiferous tubule, a reduced epithelial height indicates sloughing of spermatogenic cells or maturational arrest, whereas an increased luminal diameter also indicates maturation arrest and/or impaired spermatogenesis. For the determination of these variables, 20 nearly round seminiferous tubules are selected.

The first is selected randomly, while subsequent seminiferous tubules are selected by moving the section clockwise (Afolabi et al., 2022a; Besong et al., 2023a). The composition of the germinal cell layer can also be assessed by counting the number of germ cell layers from the basement membrane to the lumen at 90°, 180°, 270°, and 360° and taking the average of these numbers (Wei et al., 2009; Akhigbe et al., 2021b; Ogundola et al., 2021).

The distance between two seminiferous tubules may be determined as interstitial diameter or interstitial distance, indicating shrinkage of seminiferous tubules and increase of the interstitial space between two adjacent seminiferous tubules. The morphometry of the epididymis (essentially the diameter of the tubule, diameter of the lumen, epithelial height, and size of the interstitial space) is essentially performed in the same way as for the morphometry of the testis (Fig. 4).

Some histomorphometry may be calculated from the above variables. The cross-sectional area (Ac) of the seminiferous tubule is calculated as $Ac = \pi D^2/4$, where π equals 3.142 and D the mean diameter of the seminiferous tubules is calculated as outlined above (Ogedengbe et al., 2018; Afolabi et al., 2022a).

The Ac can also be determined by tracing the circumference of the seminiferous tubule (Montoto et al., 2012). The area occupied by interstitial tissue is calculated by subtracting the area occupied by seminiferous tubules from the total tissue area considered (Montoto et al., 2012).

Like a decreased diameter of the seminiferous tubules, a decrease in the Ac or percent area of the seminiferous tubules indicates shrinkage of the seminiferous tubule.

The area of the lumen of the seminiferous tubules is obtained by measuring the length and width of the lumen in each tubule and calculating the lumen area as the area of an ellipse = π x lumen length/2 (semi-major axis) x lumen width/2 (semi-minor axis), whereas the seminiferous epithelium area in each tubule is determined by subtracting the lumen area from the Ac (Montoto et al., 2012).

The unit for the diameter is µm, for area μm^2.

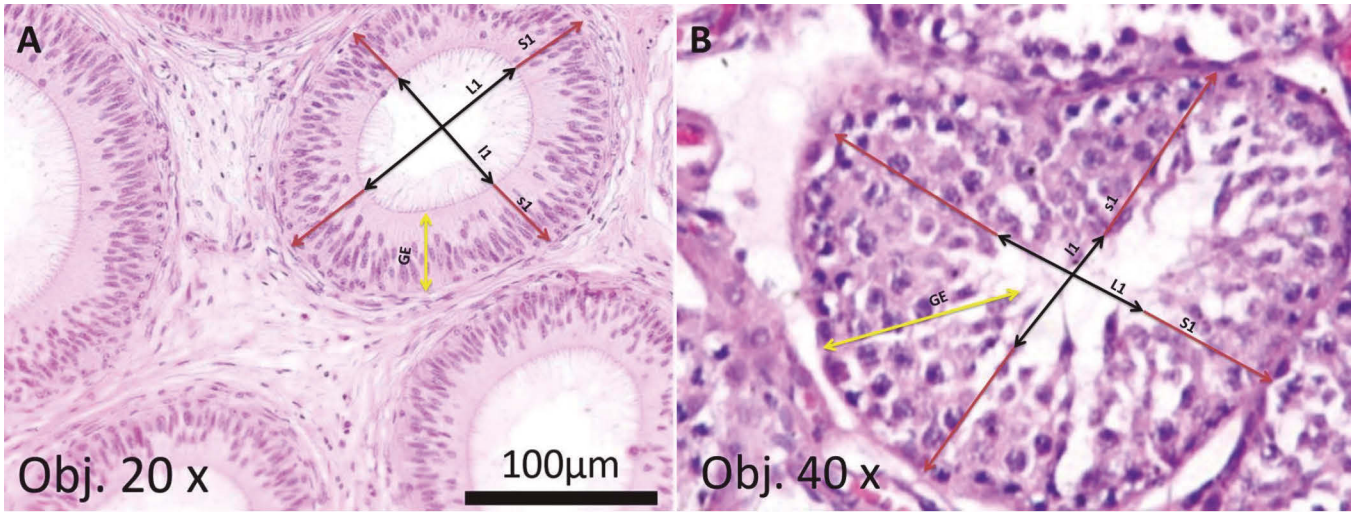

Fig. 4. Histology of the human epididymis and rabbit testis. The epididymis appears normal with normal-appearing tubules (T) and interstitial space (ISS) **(A)**. The epididymis **(A)** and testis **(B)** photomicrographs show the planimetry variables. The black lines are the diameter of the lumen, the major (L1) and minor (l1) axes, while the red lines are continuations of the black lines representing the diameter of the seminiferous tubules, the major (S1) and minor (s1) axes, and the yellow lines are the germinal epithelial height (GE). For the testicular tissue, if the number of the germinal layers is counted, it is referred to as the germ cell layer. Fig. 4A is an unpublished photomicrographs from our laboratory (Institute of Anatomy, Faculty of Medicine, University of Leipzig, Leipzig, Germany), while 4B is also from our laboratory (Reproductive Biology and Toxicology Research Laboratory, Oasis of Grace Hospital, Osogbo, Osun State, Nigeria) and have been published (Akhigbe and Ajayi, 2020).

Testicular volume (V_T, mm^3), which correlates with sperm density (Tijani et al., 2014), is obtained by dividing testicular mass by testicular density (Montoto et al., 2012). The volume of the testis occupied by the seminiferous tubules (V_{TTb}, mm^3) is calculated as V_T x percentage of total seminiferous tubules/100 (Montoto et al., 2012).

The thickness of the basement membrane and the diameter and volume of the Leydig nucleus can also be obtained, although these are better determined by an ultrastructural examination with an electron microscope at a magnification of 3,000 to 50,000x.

For basement membrane thickness (µm), ten seminiferous tubules are randomly selected and five random measurements are taken from each tubule (Pop et al., 2011; Shokri et al., 2012). The basement membrane, which is a modified extracellular matrix, appears to be involved in germ cell movement across the blood-testis-barrier; proteins in the membrane have been reported to influence the dynamics of the blood-testis-barrier of Sertoli cells through the interactions between collagens, proteases, and protease inhibitors under the influence of cytokines (Siu and Cheng, 2014). Hence, an increase in basement membrane thickness may indicate impaired spermatogenesis.

The diameter of the Leydig cell nucleus (µm) can also be measured and from this the volume of the Leydig cell nucleus (V, μm^3) can be calculated as $4/3\pi r^3$ (Castro et al., 2002; Afolabi et al., 2022a) or P/6 x AP^2 (El-Sokkary, 2001; Afolabi et al., 2022a), where r (radius) is the averaged half diameter, P the short diameter, and A the long diameter. The first formula is used for round nuclei, and the second for oval/spheroidal nuclei (Afolabi et al., 2022a).

In addition, stereological analysis has proven useful in digital pathology. It involves the collection and evaluation of tissue samples using specific protocols to obtain quantitative variables such as length, volume, and count. In this way, the degree of shrinkage, the total volume of the testis, and the volume density and absolute volume of the seminiferous tubules, germinal epithelium, and interstitial tissue can be determined. The left testis is immersed in a saline-filled glass jar to determine the weight and primary volume of the testis (Scherle, 1970), and then fixed in a buffered formaldehyde solution. This is then divided into 8-12 slabs using an orientation method to obtain Isotropic Uniform Random (IUR) sections (Mattfeldt et al., 1990) and paraffin-embedded tissue sections of 5 µm and 25 µm thickness are obtained and stained with H&E for volume and cell number estimations, respectively. Three random segments are prepared from the IUR using trocar. The average value of two vertical diameters of the segments is determined as the pre-fixing radius (r-before), while this is also repeated after histological processing and determined as the post-fixing radius (r-after). The degree of shrinkage (d (shr)) is determined as:

$D\ (shr) = 1 - (r\text{-}before^2 / r\text{-}after^2)1.5$

Post-embedding volume = Pre-embedding volume x [1 – d (shr)] (Zamani et al., 2020).

Images are captured at the same magnification and uploaded to morphometric software. About five fields per slide are evaluated by randomly superimposing a uniform point grid over the image to measure specific objects. The ratio of the number of points hitting the profile of the seminiferous tubules, germinal epithelium, and interstitial tissue (P_N) to the number of points hitting the testis (P_T) is determined as the volume density (V_D) of the seminiferous tubules, germinal epithelium, and interstitial tissue, respectively (Bielli et al., 2001).

$V_D = P_N / P_T$

The values obtained are multiplied by one hundred and expressed as percentages. The absolute volume (V_A) of the seminiferous tubules, germinal epithelium, and interstitial tissue is obtained by multiplying the corresponding V_D with the testicular weight (TW) and expressed in mL (Howard and Reed, 2004).

$V_A = V_D \times TW$

Evaluation of spermatogenesis

Spermatogenesis can be assessed using the Johnsen score, spermatogenic index, and total and daily spermatid production (Johnsen, 1970; Afolabi et al., 2022a; Akhigbe et al., 2023). The Johnsen score is based on the result of a testicular biopsy (Johnsen, 1970; Akhigbe et al., 2021a). Each seminiferous tubule evaluated is scored between 1 and 10 depending on the presence of specific spermatogenic cells (Table 2). The tubule is scored 10, 9, and 8, respectively if spermatogenesis is complete and many spermatocytes are present. When many spermatocytes are present. but the germinal epithelium is disorganized or when few spermatocytes are present. It is scored 7 and 6, respectively if no spermatocytes are present but many or few spermatids are present. In the absence of spermatozoa and spermatids, the presence of many or a few spermatocytes is scored as 5 and 4, respectively. If only spermatogonia, Sertoli cells, or no cells are present, the score is 3, 2, and 1, respectively.

When using the spermatogenic index as an indicator of spermatogenesis, the types of spermatogenic cells are also considered (Table 3). About two hundred seminiferous tubules are examined per testis, and the spermatogenic index is determined as the received value divided by two hundred.

When using total and daily spermatid production as an indicator of spermatogenesis, sonication-resistant spermatids are counted (Robb et al., 1978; Mathias et al., 2015; Akhigbe et al., 2023). The tunica albuginea is separated from the excised testis, and then the parenchyma is homogenized in 5 ml of 0.5% saline-triton by sonication at 12 kHz for 30 seconds. The homogenate is diluted in saline (1:10), and the spermatids are counted using a hemocytometer. The total spermatid production (TSP) is determined as the number of spermatids per gram of testicular tissue and expressed

as x millions per g ($x10^6$/g). The daily spermatid production (DSP) is obtained by dividing TSP by 6.1 days and expressed as million per g per day ($x10^6$/g/day).

DSP = TSP/6.1 days

The spermatids counted correspond to 48% of a seminiferous epithelial cycle that lasts 12.75 days in rats [12.75 x 0.48 = 6.1] (Robb et al., 1978; Mathias et al., 2015; Akhigbe et al., 2023).

The sonication-resistant spermatozoa in the epididymides are counted and reported as sperm reserve (Fernandez et al., 2008; Bellentani et al., 2011). The epididymal segments (caput, corpus, and cauda) are minced separately, homogenized in 5 ml of 0.5% saline-triton by sonication at 12 kHz for 30 seconds, and the homogenate is then diluted in saline (1: 10). The number of spermatozoa in the homogenate of the respective epididymal segment (caput + corpus and cauda) is counted using a hemocytometer and reported as the sperm reserve per million/organ ($x10^6$/organ). The sperm transit time (sperm transit through the epididymis) in the caput/corpus (in days) is determined by dividing the number of spermatozoa in the caput/corpus portion of the epididymis by the DSP of the ipsilateral testis, while sperm transit time (in days) in the cauda is determined by dividing the number of spermatozoa in the caudal portion of the epididymis by the DSP of the ipsilateral testis (Fernandez et al., 2008; Bellentani et al., 2011).

Leydig, Sertoli, and Spermatogenic cell counts

The counting of cells in the testicular tissue can be done manually or via applications with specific plugins, such as Image J. The cells are identified by their peculiar features. The primary, secondary, and spermatid spermatocytes are located in the adluminal compartment, which is located between the basement membrane and the lumen, while Sertoli cells and spermatogonia are located on the basal membrane (Akhigbe et al., 2023). Spermatogonia are rounded cells that locate adjacent to the basal membrane and have round nuclei. Sertoli cells are large, elongated cells that span the whole seminiferous epithelium from the basal membrane to the lumen and have oval to elongated nuclei. Primary spermatocytes have heterochromatic nuclei, whereas secondary spermatocytes lie between the primary spermatocytes and round spermatids. Sometimes, the primary and secondary spermatocytes are counted together and reported as spermatocytes. Leydig cells are located in clusters in the space between the seminiferous tubules. They are polyhedral eosinophilic cells that have a large, round nucleus with one to three nucleoli (Fig. 1). Cell counts should be performed by two experts, who are unaware of the study protocol, and the respective mean values of their counts should be used.

Assessment of sperm morphology

Sperm morphology, which refers to the shape and size of sperm, is a widely used method for determining sperm quality. This method is based on the distinctive staining of spermatozoa (Maree et al., 2010) and is a component in the diagnosis of male infertility. Due to increasing IVF (*in vitro* fertilization) treatments, the

Table 2. Johnsen's grading for testicular biopsy.

Grade	Features observed
1	No cells (either germ cell or Sertoli cell) in the tubular section
2	No germ cells but Sertoli cells are present
3	Spermatogonia are the only germ cells present
4	Only a few spermatocytes (<5) and no spermatids or spermatozoa present
5	No spermatozoa or spermatids but several or many spermatocytes present
6	No spermatozoa and only a few spermatids (<5-10) present
7	No spermatozoa but many spermatids present
8	Only a few spermatozoa (<5-10) present
9	Many spermatozoa present but disorganized germinal epithelium
10	Complete spermatogenesis with many spermatozoa

Johnsen, 1970; Akhigbe et al., 2021a.

Table 3. Spermatogenic index for scoring spermatogenesis.

Grade	Features observed
1	Only spermatogonia present
2	Spermatogonia and spermatocytes present
3	Spermatogonia, spermatocytes, and round (early) spermatids present with
4	Spermatogonia, spermatocytes, and round spermatids present with up to 25 late spermatids per tubule

Akhigbe et al., 2021a; Afolabi et al., 2022a.

shape and size of sperm are gaining importance in terms of their usability in artificial insemination (Aksoy et al., 2012). However, there is no universal technique that covers the wide range of indications (fertility diagnosis and prognosis, reproductive toxicology studies, empirical studies, or public health studies) for which human sperm morphology studies are used (Aksoy et al., 2012). In addition, some shape anomalies of unclear etiology, such as narrow heads, amorphous heads, and curved or asymmetric necks, also appear to be without disease and/or fertility reduction value (Gatimel et al., 2017).

The World Health Organization (WHO) laboratory handbook for semen analysis recommends using the so-called stringent approach to determine the proportion of spermatozoa with a perfect shape (WHO, 2021). Several criteria must be examined and met for the diagnosis of male infertility (Boitrelle et al., 2021), however, sperm morphology is very difficult to interpret due to the physiological nature of most morphological sperm abnormalities. With the exception of easily diagnosable morphological changes in very rare genetic disorders (such as globozoospermia, macrocephaly, decapitated sperm syndrome, and fibrous envelope dysplasia), sperm morphology assessment in the context of assisted reproductive therapy (ART) contributes little to diagnosis and treatment (Gatimel et al., 2017). In the absence of reliable morphological criteria, more and more infertility clinics rely on other criteria in the spermiogram to assess sperm fertilizability and plan treatment strategies (Abu Hassan Abu et al., 2012). However, assessment of sperm concentration and motility may also provide inaccurate results, even when used alongside sperm morphology to assess the fertility of a semen sample (Chacon, 2001). Several staining approaches are used in sperm morphology evaluation (Aksoy et al., 2012). Automated devices for sperm morphology analysis can compensate for the subjective nature of the visual assessment of sperm morphology, however, there are numerous technical problems (Ombelet et al., 1995).

Ejaculatory abstinence of 2-7 days (WHO, 2021; Akhigbe et al., 2022a) or 3-4 days (European Society for Human Reproduction and Embryology [ESHRE] and the Nordic Andrology Association [NAA]) is recommended prior to collection of semen samples for testing (Tremellen, 2008; Akhigbe et al., 2022a). The suggested period of 2-7 days of abstinence prior to semen collection is intended to reduce the intrusion into the individual's life and habits (Björndahl et al., 2022). Studies have shown that a prolonged abstinence period would increase sperm count but not motility (Akhigbe et al., 2022a; Björndahl and Brown, 2022), and sperm morphology has been shown to be similar with an ejaculatory abstinence of 3-4 and 2-7 days (Akhigbe et al., 2022a). To determine sperm morphology, a sperm smear is made on a glass slide, air-dried, fixed, and stained with eosin/nigrosin. The slide is examined with a light microscope after being covered with a glass coverslip. Approximately 200 spermatozoa per slide are examined for normal and abnormal forms.

The variable shapes of human spermatozoa make evaluation quite difficult, nevertheless, assessment of spermatozoa from the female reproductive tract, particularly from post-coital endocervical mucus and from the surface of the zona pellucida, has improved our understanding of what morphologically normal and potentially fertilizing spermatozoa are (WHO, 2021).

The spermatozoa consist of a head, neck, mid piece (middle piece), principal piece, and end piece. However, it is difficult to view all pieces with a light microscope, so spermatozoa are described to have a head (and neck) and a tail (mid piece and principal piece) (WHO, 2021). In humans, the head should be oval-shaped, smooth, and regular in shape with a well-defined acrosomal region that accounts for about 40-70% of the head area, while the mid piece should be slender, regular, and approximately as long as the sperm head.

The longitudinal axis (major axis) of the mid piece should coincide with that of the head. The principal piece should be thinner than the mid piece with a uniform caliber and about 10 times longer than the sperm head. Normally, the principal piece is about 45 μm long. Defects in the head include a large or small head, a round, pyriform, tapered, amorphous, or vacuolated head (more than two vacuoles or 20% of the head area occupied by unstained vacuolar areas), vacuoles in the postacrosomal region, large (>70% of the head area) or small (<40% of the head area) acrosomal areas, double head, or a combination of these (WHO, 2021). Asymmetrical insertion of the mid piece into the head, unusually thin, thick, or irregular, abruptly bent, or a combination of these are examples of defects in the neck and mid piece. Short, numerous, broken, smooth hairpin bends, sharply angulated bends, irregular breadth, coiling, or any combination of these are examples of defects in the principal piece.

To evaluate DNA damage in the sperm head, the slide may be stained with aniline blue (Ajayi and Akhigbe, 2020d) or toluidine blue (Akhigbe et al., 2023). Sperm heads stained light blue or blue have intact DNA but those stained dark blue have damaged DNA. Figure 5 shows the sperm cells of a rat and a human.

Histopathological evaluation of the ovary and uterus

Qualitative report

Histological sections of the ovaries are usually examined under a light microscope at 100x magnification (Obj. 10x), however, a higher magnification, such as 400x (Obj. 40x), may be required to view specific lesions. The abnormalities observed in ovarian tissues vary from the presence of polycystic ovaries (seen in Polycystic Ovarian Syndrome, PCOS) to degeneration of follicles and/or corpus lutea, infiltration of inflammatory cells, vascular congestion, abundant atretic follicles, and cellular hyperplasia, hypertrophy,

metaplasia, dysplasia, or atrophy (Fig. 6). Usually, an adverse exposure may induce one or more of these pathological changes, although some may be pathognomonic for a disorder. Ovarian ischemia/reperfusion (I/R) injury, caused by ovarian torsion/detorsion, may lead to distortion of the ovarian histoarchitecture with noticeable features like vascular congestion, infiltration of inflammatory cells, edema, hemorrhage, and atretic follicles (Yigiter et al., 2011; Akhigbe et al., 2022b). In animal models, PCOS presents with cystic follicles, atretic oocytes, and empty follicles (Bafor et al., 2021).

Anomalies observed in the uterine tissue may include vascular congestion, hemorrhage, atrophy, hypertrophy or hyperplasia of the uterine glands, increased or reduced diameter of the endometrial lumen, edema, infiltration of inflammatory cells, and the presence of tumors.

Semi-quantitative and quantitative report

For an appropriate comparison, it may be important to quantify the lesions observed in ovarian tissues. This allows objective evaluation of the effect of an exposure. A semiquantitative scoring may be useful. In this case, lesions observed, such as follicular degeneration, vascular congestion, edema, hemorrhage, and infiltration of inflammatory cells are scored as 0, 1, 2, and 3 to indicate the absence or presence of about <33%, 33-66%, and >66% of each of these lesions, respectively (Guven et al., 2010; Akhigbe et al., 2022b).

At least five replicates per group are scored independently by two experts blinded to the study protocol, and the average score is determined and used for each slide. The number of healthy follicles and atretic follicles, and the ratio between them, can also be counted and reported. In general, a follicle is considered 'atretic' if at least two of the following features are present: increased pyknotic nuclei in the granulosa cell layer, cell debris within the antral cavity, granulosa cells pulling away from the basement membrane, swelling in theca cells, degenerating oocyte, and degenerated zona pellucida (Afolabi et al., 2022b; Akhigbe et al., 2022b). Similarly, the presence of vascular congestion, edema, hemorrhage, and infiltration of inflammatory cells in uterine tissue may also be graded as 0, 1, 2, and 3 to depict the absence or presence of about <33%, 33-66%, and >66% of each of these lesions, respectively.

As in testicular tissues, ovarian and uterine planimetry are also useful tools. Variables that can be determined in ovarian tissues include oocyte diameter (μm), theca layer thickness (μm), mural granulosa layer thickness (μm), and thickness of the corpus luteum (μm), while variables that can be assessed in uterine tissues include endometrial thickness (μm), myometrial thickness (μm), uterine gland diameters (μm), and endometrial lumen diameter (μm).

In addition, folliculogenesis/oogenesis may be evaluated by counting the different follicles; primordial follicles, primary follicles, secondary preantral follicles, tertiary antral follicles, and preovulatory Graafian follicles (2 cm in diameter in human) (Afolabi et al., 2022b; Akhigbe et al., 2022b). The follicles may be counted manually or by using Image J software. The follicles are easily identified by their particular characteristics, as described earlier in section 2.2.

Stereological analysis is also a beneficial tool in the evaluation of ovarian tissues. The ovary is divided into IUR sections. The ovarian tissue is blocked in a cylindrical paraffin block and is randomly placed on the φ-clock, then each half of this is divided into nine equal segments, from which a number from 1 to 9 is randomly picked. The block is then placed on the θ-clock and each half of it is divided into nine unequal sine-weighted parts along the cut surface on the θ-θ axis. Then a cut is made along a randomly chosen number and consecutive 5- and 20-μm thick sections are prepared with a microtome and then stained with H&E. The volume of the ovary, cortex, medulla, and corpus luteum may be determined using Cavalieri's principle (Gundersen et al., 1988a,b):

$V\text{total}=\Sigma pxa/pxt$

Where Σp=total number of points superimposed on the image

t=thickness of the section

a/p=area associated with each point

The total number of each follicle and granulosa cells may be determined using an optical dissector as reported earlier (Gundersen et al., 1988a,b). The numerical density (Nv) of each follicle (primordial, primary,

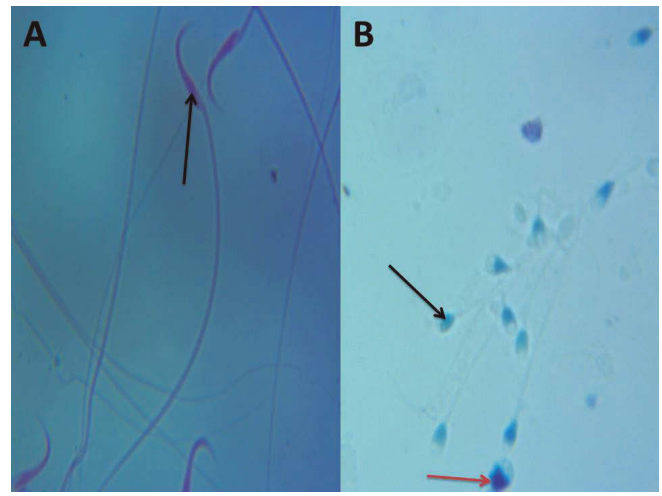

Fig. 5. Photomicrographs of the sperm morphology of a rat **(A)** and human **(B)**. The sperm head of the rat (black arrow, **A**) is faciform-shaped (or talons) and composed of the nucleus, acrosomic system, perinuclear theca, and plasma membrane. The sperm head in humans (black and red arrow, **B**) is oval-shaped and contains a densely-compact nucleus that is capped by acrosome and plasma membrane. Fig. 5B is stained with Toluidine blue. Sperm heads stained light blue or blue are DNA with intact integrity (black arrow), while those stained dark blue were considered those with damaged DNA (red arrow). Fig. 5A and B are unpublished photomicrographs from our laboratory (The Brainwill Laboratory, Osogbo, Osun State, Nigeria).

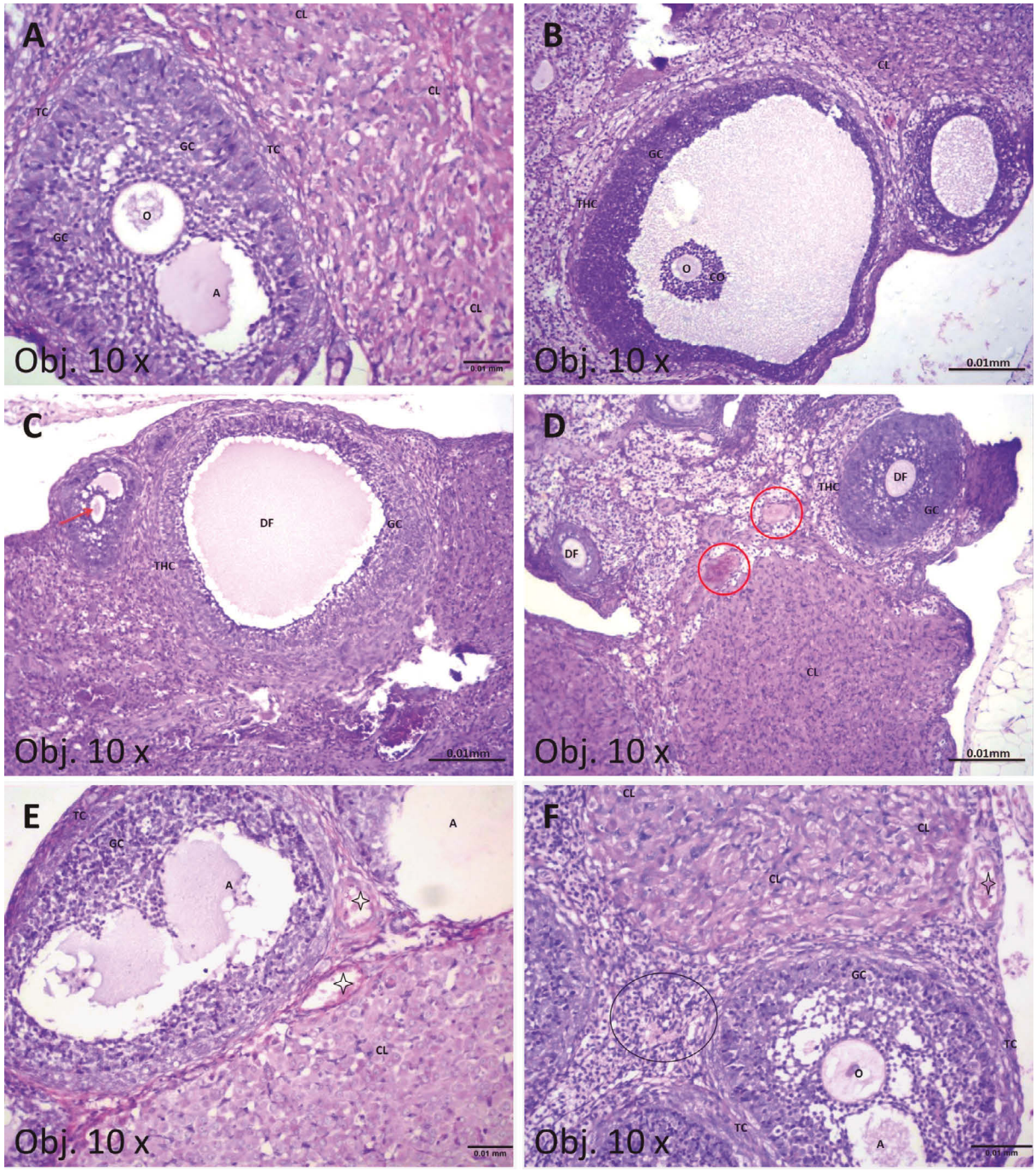

Fig. 6. Histology of the ovary of a Wistar rat **(A)** and corpus luteum **(B)**, and the ovary of a Wistar rat **(C)** showing normal histoarchitecture. **A, B.** Show normal ovarian tissues with preserved ovarian outer cortex and inner medulla. The cortical region is composed of follicles at varying degree of maturity. The graafian follicle is lined by cubiodal epithelium and contained a matured oocyte (O) with a defined zona pellucida, zonal granulosa (GC), corona radiata (CR), antrum (A) and defined theca follicular cells (TC, THC). The medulla contained blood vessels and lymphatics. The corpus luteum (CL) appeared unremarkable. Fig. 6C-F show ovarian tissues with distorted histoarchitecture. **C.** Shows some degenerated follicles (DF) and some developing ooctes (red arrow). The granulosa cell (GC) and theca cells (THC) appeared normal. **D.** Shows degenerated follicles (DF) with distorted granulosa cell (GC) and theca cells (THC) that appeared infiltrated by inflammatory cells. The interstitium appeared congested (red circle). **E.** Shows follicles at varying degree of maturity, and are predominantly degenerating follicles (A) lined by cubiodal epithelium and theca follicular cells (TC). The medulla contains blood vessels, and the interstitium appeared congested (star) with inflammatory cell infiltration. The corpus luteum (CL) appears inconspicuous. **F.** Shows follicles at varying degree of maturity and are predominantly healthy (circle). The follicle was lined by cuboidal epithelium and contained defined theca follicular cells (TC). The medulla contained blood vessels (arrow), and the interstitium appear markedly congested (star) with inflammatory cell infiltration (oval). The corpus luteum (CL) appears unremarkable. Fig. 6A, E, and F are photomicrographs from our laboratory (Reproductive Biology and Toxicology Research Laboratory, Oasis of Grace Hospital, Osogbo, Osun State, Nigeria) and has been published (Akhigbe et al., 2022b). Fig. 6B, C, and D are photomicrographs from our laboratory (Reproductive Biology and Toxicology Research Laboratory, Oasis of Grace Hospital, Osogbo, Osun State, Nigeria) and has been published (Afolabi et al., 2022b).

secondary, and antral) and granulosa cell is estimated as: $Nv=(\Sigma Q)/(\Sigma Pxhxa/f)xt/BA$

Where ΣQ=number of nuclei, ΣP=total number of unbiased counting frames in all fields, h=height of the dissector, a/f= frame area, t= real section thickness measured in every field using microcator, and BA=block advance of the microtome.

The total number of these cells may be determined as:

$Ntotal=Nv$ x V

The volume of the oocytes (V) is determined as: $V=4/3\pi xLn^3$. Where Ln=distance from the center of the nucleolus to the oocyte membrane.

Stereological analysis may also be useful in the evaluation of the uterus. To determine uterine volume, the uterine horn is divided into 8 to 12 parallel sections at a specific distance (t). The area around each point is determined as $a(p) =\Delta X$ x ΔY, then the area of each slice is determined by multiplying the total number of the points on the grid hitting the slides, $\sum_{i=1}^{n} P$

The total volume of the uterine horn is then determined as:

$$V_{\text{total uterine horn}}=\sum_{i=1}^{n} xa(p)xt$$

The volume density of the structures of interest, such as the perimetrium, myometrium, endometrium, lumen, and uterine glands may be determined on a 5-µm thick section using Delesse's formula (Noorafshan et al., 2013):

$$Vv(\text{structure})=\sum_{i=1}^{n} P\ (\text{structure})\ X=\sum_{i=1}^{n} P\ (\text{reference})$$

Where $\sum_{i=1}^{n} P$ (structure)=the number of test points falling on the targeted structure and $\sum_{i=1}^{n} P$ (reference)=the total points hitting the uterine horn sections.

The volume of the absolute targeted structure is determined as:

V(structure) =V total uterine horn x Vv (structure)

Histopathological evaluation of other reproductive organs

Apart from the testes and epididymides (in males) and ovaries and uterus (in females), the seminal vesicles, prostate, and penis (in males) and fallopian tubes and vagina (in females) contribute greatly to fertility. Disruption of the histoarchitecture of any of these organs can lead to dysfunction and consequent fertility impairment. Figure 8 shows the histology of these organs in healthy and diseased states. Anomalies that may occur after harmful exposure include cellular hyperplasia, hypertrophy or atrophy, thickening or thinning of the epithelial lining, focal hemorrhagic lesion, vascular congestion, and narrowing or widening of the lumen.

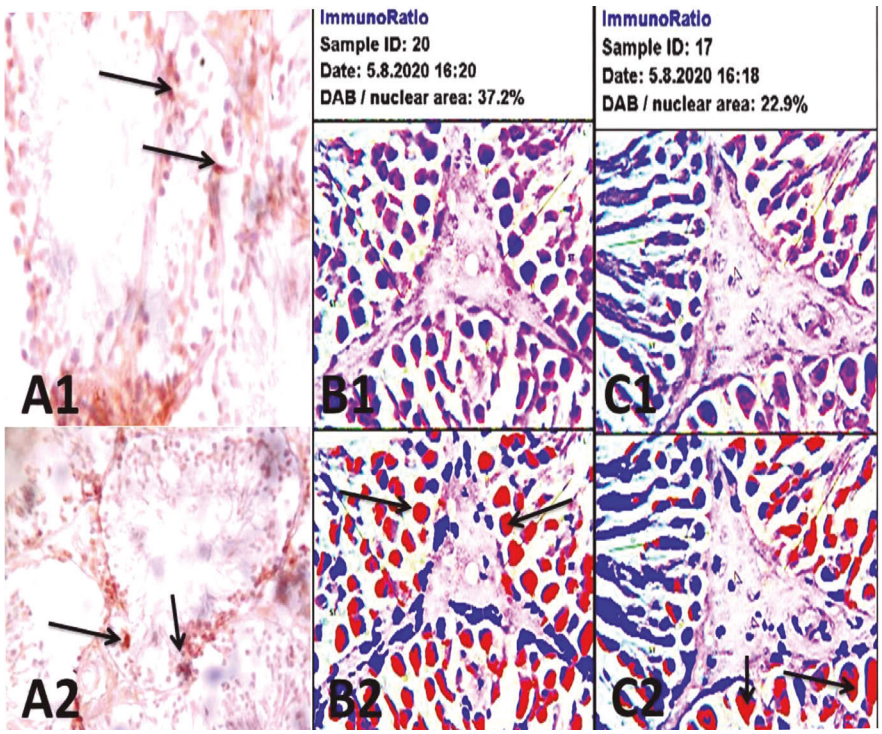

Fig. 7. Photomicrographs of testicular tissues showing the expression of caspase 3 **(A1, A2)** and Bcl-2 **(B1, B2, C1, C2)** by IHC. The development of diaminobenzidine molecule (DAB) as an enzymatic substrate yields a stable brown product, indicating the immunopositivity. The immune-positive cells appear brown (black arrow) **(A1, A2)** or red **(B2, C2)** in pseudo images. B2 is the pseudoimage of B1, while C2 is the pseudoimage of C1. Fig. 7A1 and A2 are unpublished photomicrographs from our laboratory (Reproductive Biology and Toxicology Research Laboratory, Oasis of Grace Hospital, Osogbo, Osun State, Nigeria). Fig. 7B1, B2, C1 and C2 are photomicrographs from our laboratory (Reproductive Biology and Toxicology Research Laboratory, Oasis of Grace Hospital, Osogbo, Osun State, Nigeria) and has been published (Ajayi and Akhigbe, 2020b).

These anomalies can be used to grade the damage/injury to any of these organs. The presence of vascular congestion, edema, hemorrhage, and infiltration of inflammatory cells in these tissues can also be graded as 0, 1, 2, and 3, respectively, to indicate the absence or presence of about <33%, 33-66%, and >66% of each of these lesions and to provide semi-quantitative data. In addition, quantitative data can be obtained by

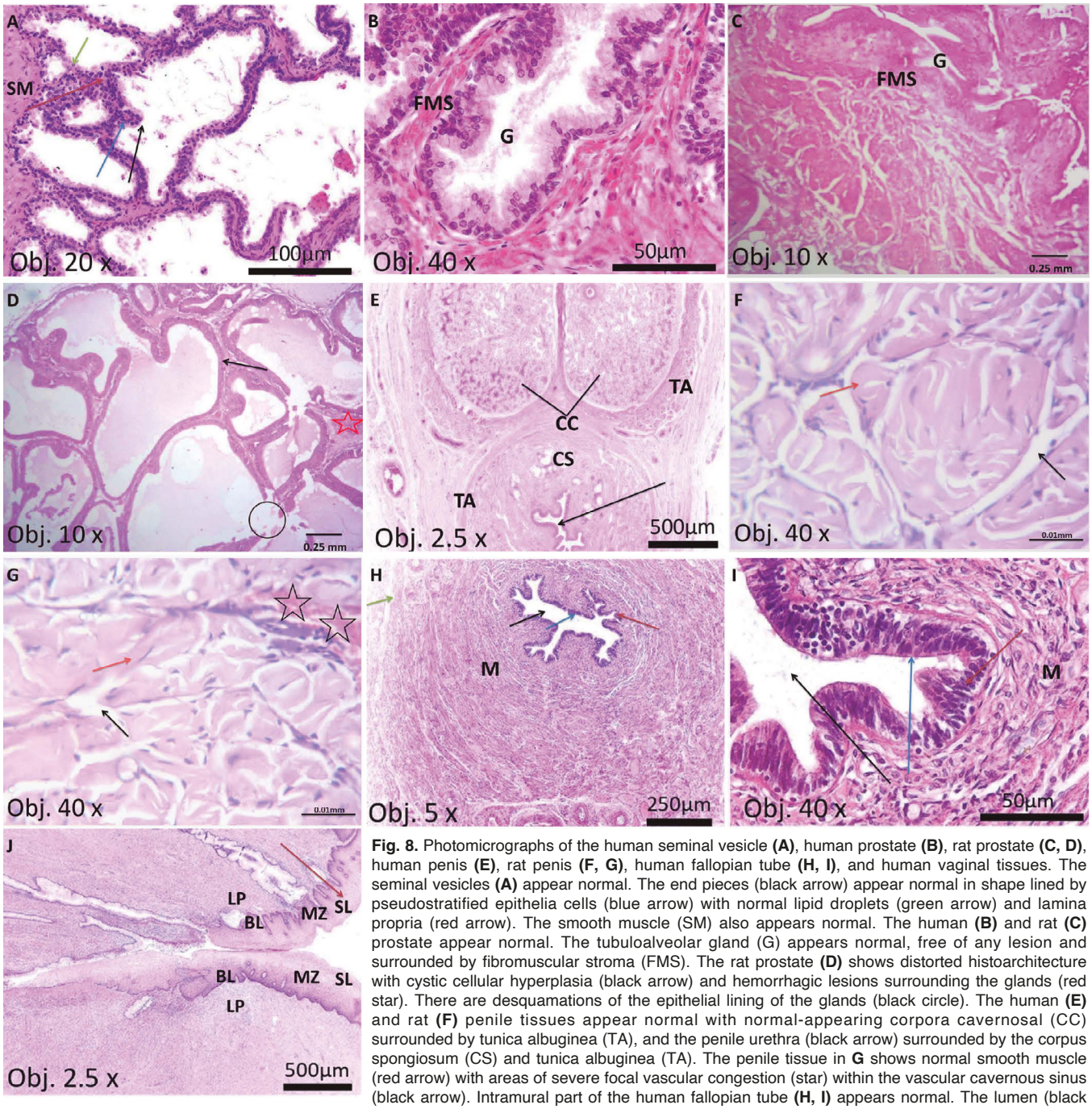

Fig. 8. Photomicrographs of the human seminal vesicle **(A)**, human prostate **(B)**, rat prostate **(C, D)**, human penis **(E)**, rat penis **(F, G)**, human fallopian tube **(H, I)**, and human vaginal tissues. The seminal vesicles **(A)** appear normal. The end pieces (black arrow) appear normal in shape lined by pseudostratified epithelia cells (blue arrow) with normal lipid droplets (green arrow) and lamina propria (red arrow). The smooth muscle (SM) also appears normal. The human **(B)** and rat **(C)** prostate appear normal. The tubuloalveolar gland (G) appears normal, free of any lesion and surrounded by fibromuscular stroma (FMS). The rat prostate **(D)** shows distorted histoarchitecture with cystic cellular hyperplasia (black arrow) and hemorrhagic lesions surrounding the glands (red star). There are desquamations of the epithelial lining of the glands (black circle). The human **(E)** and rat **(F)** penile tissues appear normal with normal-appearing corpora cavernosal (CC) surrounded by tunica albuginea (TA), and the penile urethra (black arrow) surrounded by the corpus spongiosum (CS) and tunica albuginea (TA). The penile tissue in **G** shows normal smooth muscle (red arrow) with areas of severe focal vascular congestion (star) within the vascular cavernous sinus (black arrow). Intramural part of the human fallopian tube **(H, I)** appears normal. The lumen (black arrow) is free of any collection or lesion and lined with secretory simple ciliated columnar epithelial cells (blue arrow) and connective tissues (red arrow). The muscular wall (M) appears normal. Endo- and ectocervix **(J)** appears normal with the cavity surrounded by squamous epithelium with the superficial layer (SL), mid zone (MZ), and basal layer (BL). The lamina propria (LP) also appears normal. Fig. 8A, B, E, H, I and J are unpublished photomicrographs from our laboratory (Institute of Anatomy, Faculty of Medicine, University of Leipzig, Leipzig, Germany), while Fig. 8C, D (unpublished), F, and G (published, Besong et al., 2023b) (Reproductive Biology and Toxicology Research Laboratory, Oasis of Grace Hospital, Osogbo, Osun State, Nigeria and The Brainwill Laboratory, Osogbo, Osun State, Nigeria).

determining the lumen diameter (μm) of a gland or cavity or the thickness of an epithelium (μm) or a muscle layer (μm).

Immunohistochemistry

Immunohistochemistry (IHC) can be particularly useful in assessing variables that can also be examined using laboratory techniques, such as Enzyme-Linked Immunosorbent Assay (ELISA) or Polymerase Chain Reaction (PCR). In addition to these methods, IHC provides a microscopic picture of the affected cell(s). The tissue can be processed as previously reported (Ajayi and Akhigbe, 2020b). Tissue fixed in formalin and embedded in paraffin is sectioned at 4 μm. After deparaffinization and rehydration of the sections, antigens are retrieved in heated citrate buffer and sections are then allowed to cool for 30 minutes. After cleaning the slides with Kim wipes and circling the section area with a hydrophobic pen, the slides are placed in a humidified chamber. Endogenous peroxidase activity is blocked with hydrogen peroxide for 10 minutes. After rinsing once with PBS, an ultra V protein block is applied to the slides and allowed to incubate for 10 minutes. The slides are then rinsed twice with PBS, and the appropriate primary antibodies are applied (i.e., anti-mouse caspase 3 monoclonal for caspase 3 expression, 1:200 or anti-mouse Bcl-2 monoclonal for Bcl-2 expression, 1:200).

After 45 minutes of incubation at room temperature, the slides are rinsed twice with PBS before the species-matched biotinylated secondary antibody is applied. The slides are then incubated for another 25 minutes at room temperature, rinsed twice with PBS, and HRP polymer is added for 25 min. After two more PBS rinses, the sections are incubated in diaminobenzidine (DAB) substrate for 5 minutes before being rinsed twice with PBS, counterstained with eosin, and coverslipped for qualitative analysis.

The labeled cell nuclei appear brownish, indicating binding of the antibody to the targeted nuclear antigen. For quantification, captured photomicrographs are imported into Image J software with specific plugins. ImmunoRatio pseudo images are generated and the proportion of DAB-stained area is evaluated as reported earlier (Tuominen et al., 2010; Ajayi and Akhigbe, 2020b). The inputs received include a microscope image, an optional blank-field correction image, and thresholding adjustment parameters, then the Rolling Ball algorithm is employed for background subtraction. The Colour Deconvolution plugin is employed to separate the stains into two eight-bit component images, DAB precipitation and hematoxylin counterstaining (H), which are then processed with a mean filter and binarized using adaptive IsoData thresholding.

Component-specific threshold adjustments are made for smooth threshold output and processed with a median filter. The Watershed algorithm is used to segment the nuclei of both components, and small particles are removed based on their size. Thin (fibroblastic) cells are detected and removed for the H component by removing non-round particles. The H and DAB components are overlaid on the initial image, and then the percentage of DAB-stained nuclear area out of the total nuclear area (the labeling index) is calculated. The results are presented in "percent" or "normalized with the control group".

Conclusion and future perspectives

Histopathological evaluation of the reproductive organs is a valuable tool in the diagnosis of infertility. Although its use is limited in humans because of its invasive nature, at least sperm morphology is a useful component of conventional semen analysis that provides information on semen quality. However, in animal models, the importance of histopathological examinations of reproductive organs cannot be overestimated. It provides useful information predictive of the organ's integrity, germ cell formation, and sex steroid hormone synthesis. It also provides mechanistic information on the pathogenesis of disease models or harmful exposures. Despite the technical expertise required, which can be a limiting factor, it remains an indispensable tool.

Ethical Approval. The research was approved by the institution's Ethics Review Committee, Ethical Review Committee, Oasis of Grace Hospital, Nigeria (Approval number: OGH/2022/437).

Competing Interests. The authors have no conflicts of interest.

Authors' Contributions. Conceptualization and design: REA. Funding acquisition: AMR, MAH, and REA. Investigation: AMR, MAH, and REA. Methodology: AMR, MAH, and REA. Project administration: AMR, MAH, and REA. Supervision: REA. Validation: AMR, MAH, and REA. Writing-original draft: AMR, MAH, and REA. Writing-review and editing and final approval: AMR, MAH, and REA.

Funding. This study was self-funded.

Data Availability. The data used to support the findings of the present study are available from the corresponding author upon request.

References

Abu Hassan Abu D., Franken D.R., Hoffman B. and Henkel R. (2012). Accurate sperm morphology assessment predicts sperm function. Andrologia 44, 571-577.

Afolabi O.A., Anyogu D.C., Hamed M.A., Odetayo A.F., Adeyemi D.H. and Akhigbe R.E. (2022a). Glutamine prevents upregulation of NF-kB signaling and caspase 3 activation in ischaemia/reperfusion-induced testicular damage: An animal model. Biomed. Pharmacother. 150, 113056.

Afolabi O.A., Hamed M.A., Anyogu D.C., Adeyemi D.H., Odetayo A.F and Akhigbe R.E. (2022b). Atorvastatin-mediated downregulation of VCAM-1 and XO/UA/caspase 3 signaling averts oxidative damage and apoptosis induced by ovarian ischaemia/reperfusion injury. Redox Rep. 27, 212-220.

Ajayi A.F. and Akhigbe R.E. (2020a). Staging of the estrous cycle and induction of estrus in experimental rodents: an update. Fertil. Res.

Pract. 6, 1-5.
Ajayi A.F. and Akhigbe R.E. (2020b). *In vivo* exposure to codeine induces reproductive toxicity: role of HER2 and p53/Bcl-2 signaling pathway. Heliyon 6, e05589.
Ajayi A.F. and Akhigbe R.E. (2020c). The physiology of male reproduction: Impact of drugs and their abuse on male fertility. Andrologia 52, e13672.
Ajayi A.F. and Akhigbe R.E. (2020d). Codeine-induced sperm DNA damage is mediated predominantly by oxidative stress rather than apoptosis, Redox Rep. 25, 33-40.
Ajayi A.F., Oluwole D.T., Akhigbe R.E., Hamed M.A. and Ajayi L.O. (2023). Proton pump dysfunction and upregulation of caspase-3 activity via oxidative-sensitive signaling mediate rohypnol-induced testicular toxicity. Andrologia 2023.
Akhigbe R. and Ajayi A. (2020). Testicular toxicity following chronic codeine administration is via oxidative DNA damage and up-regulation of NO/TNF-α and caspase 3 activities. PLoS One 15, e0224052.
Akhigbe R.E,. Hamed M.A. and Aremu A.O. (2021a). HAART exacerbates testicular damage and impaired spermatogenesis in anti-Koch-treated rats via dysregulation of lactate transport and glutathione content. Reprod. Toxicol. 103, 96-107.
Akhigbe R.E., Hamed M.A., Odetayo A.F., Akhigbe T.M., Ajayi A.F. and Ajibogun F.A. (2021b). Omega-3 fatty acid rescues ischaemia/perfusion-induced testicular and sperm damage via modulation of lactate transport and xanthine oxidase/uric acid signaling. Biomed. Pharmacother. 142, 111975.
Akhigbe R.E., Hamed M.A., Dutta S. and Sengupta P. (2022a). Influence of ejaculatory abstinence period on semen quality of 5165 normozoospermic and oligozoospermic Nigerian men: a retrospective study. Health Sci. Rep. 5, e722.
Akhigbe R.E., Ebiwonjumi O.S., Ajayi L.O. and Ajayi A.F. (2022b). Codeine alters female reproductive function by targeting ovarian steroidogenesis and folliculogenesis via the induction of oxidative stress, inflammation, and apoptosis. Reprod. Toxicol. 109, 1-9.
Akhigbe R.E., Afolabi O.A. and Ajayi A.F. (2023). L-Arginine abrogates maternal and pre-pubertal codeine exposure-induced impaired spermatogenesis and sperm quality by modulating the levels of mRNA encoding spermatogenic genes. Front. Endocrinol. 14, 1180085.
Aksoy E., Aktan T.M., Duman S. and Cuce G. (2012). Assessment of spermatozoa morphology under light microscopy with different histologic stains and comparison of morphometric measurements. Int. J. Morphol. 30, 1544-1550.
Arnold W.N. (2018). Autolysis. In: Yeast cell envelopes: biochemistry, biophysics, and ultrastructure. CRC Press. pp 129-137.
Auger J. (2010). Assessing human sperm morphology: top models, underdogs or biometrics? Asian J. Androl. 12, 36-46.
Babaei M., Alizadeh-Fanalou S., Nourian A., Yarahmadi S., Farahmandian N., Nabi-Afjadi M., Alipourfard I. and Bahreini E. (2021). Evaluation of testicular glycogen storage, FGF21 and LDH expression and physiological parameters of sperm in hyperglycemic rats treated with hydroalcoholic extract of Securigera Securidaca seeds, and Glibenclamide. Reprod. Biol. Endocrinol. 19, 104.
Bafor E.E., Uchendu A.P., Osayande O.E., Omoruyi O., Omogiade U.G., Panama E.E., Elekofehinti O.O., Oragwuncha E.L. and Momodu A. (2021). Ascorbic acid and alpha-tocopherol contribute to the therapy of Polycystic Ovarian Syndrome in mouse models. Reprod. Sci. 28, 102-120.
Baker J.R. (1958). Principles of biological microtechnique. A study of fixation and dyeing. Principles of biological microtechnique. A study of fixation and dyeing. Franklin Classics Trade Press, USA.
Barteczko K.J. and Jacob M.I. (2000). The testicular descent in human. Origin, development and fate of the gubernaculum Hunteri, processus vaginalis peritonei, and gonadal ligaments. Adv. Anat. Embryol. Cell. Biol. 156, 1-98.
Bellentani F.F., Fernandes G.S., Perobelli J.E., Pacini E.S., Kiguti L.R., Pupo A.S. and Kempinas W.D. (2011). Acceleration of sperm transit time and reduction of sperm reserves in the epididymis of rats exposed to sibutramine. J. Androl. 32, 718-724.
Bellofiore N., Ellery S.J., Mamrot J., Walker D.W., Temple-Smith P. and Dickinson H. (2017). First evidence of a menstruating rodent: the spiny mouse (*Acomys cahirinus*). Am. J. Obstet. Gynecol. 216, 40.e1-40.e11.
Besong E.E., Ashonibare P.J., Obembe O.O., Folawiyo M.A., Adeyemi D.H., Hamed M.A., Akhigbe T.M. and Akhigbe R.E. (2023a). Zinc protects against lead-induced testicular damage via modulation of steroidogenic and xanthine oxidase/uric acid/caspase 3-mediated apoptotic signaling in male Wistar rats. Aging Male 26, 2224428.
Besong E.E., Ashonibare P.J., Akhigbe T.M., Obimma J.N. and Akhigbe R.E. (2023b). Sodium acetate abates lead-induced sexual dysfunction by upregulating testosterone-dependent eNOS/NO/cGMP signaling and activating Nrf2/HO-1 in male Wistar rat. Naunyn. Schmiedebergs Arch. Pharmacol. 1-11.
Bielli A., Katz H., Pedrana G., Gastel M.A.T., Morana A., Castrillejo A., Lundeheim N., Forsberg M. and Rodriguez-Martinez H. (2001). Nutritional management during fetal and postnatal life, and the influence on testicular stereology and Sertoli cell numbers in Corriedale ram lambs. Small Rumin. Res. 40, 63-71.
Björndahl L. and Brown J.K. (2022). The sixth edition of the WHO Laboratory Manual for the Examination and Processing of Human Semen: ensuring quality and standardization in basic examination of human ejaculates. Fertil. Steril. 117, 246-251.
Boitrelle F., Shah R., Saleh R., Henkel R., Kandil H., Chung E., Vogiatzi P., Zini A., Arafa M. and Agarwal A. (2021). The sixth edition of the WHO manual for human semen analysis: a critical review and SWOT analysis. Life 11, 1368.
Bolon B., Dostal L.A. and Garman R.H. (2021). Neuropathology evaluation in juvenile toxicity studies in rodents: Comparison of developmental neurotoxicity studies for chemicals with juvenile animal studies for pediatric pharmaceuticals. Toxicol. Pathol. 49, 1405-1415.
Brower M. (2018). Overview of the reproduction of laboratory mice and rats. In: Encyclopedia of reproduction. Second Edition. Skinner M.K. (ed). Academic Press. pp 711-721.
Carretero A., Ruberte J. and Navarro M. (2017). Female genital organs. In: Morphological mouse phenotyping. Ruberte J., Carretero A. and Navarro M. (eds). Academic Press. pp 227-251.
Castro A., Berndtson W. and Cardoso F. (2002). Plasma and testicular testosterone levels, volume density and number of Leydig cells and spermatogenic efficiency of rabbits. Braz. J. Med. Biol. Res. 35, 493-498.
Chacon J. (2001). Assessment of sperm morphology in zebu bulls, under field conditions in the tropics. Reprod. Domest. Anim. 36, 91-99.
Chaffin C.L. and VandeVoort C.A. (2013). Follicle growth, ovulation, and luteal formation in primates and rodents: A comparative perspective. Exp. Biol. Med. 238, 539-548.

Comanescu M., Annaratone L., D'Armento G., Cardos G., Sapino A. and Bussolati G. (2012). Critical steps in tissue processing in histopathology. Recent Pat. DNA Gene Seq. 6, 22-32.

Cosentino M.J., Nishida M., Rabinowitz R. and Cockett A.T. (1985). Histological changes occurring in the contralateral testes of prepubertal rats subjected to various durations of unilateral spermatic cord torsion. J. Urol. 133, 906-911.

Cunha G.R., Sinclair A., Ricke W.A., Robboy S.J., Cao M. and Baskin L.S. (2019). Reproductive tract biology: Of mice and men, Differentiation 110, 49-63.

Del Vecchio F. (1981). The early development of the cranial segment of the müllerian duct in the rat. Morphol. Med. 1, 73-81 (In German).

El-Sokkary G.H. (2001). Quantitative study on the effects of chronic ethanol administration on the testis of adult male rat. Neuro Endocrinol. Lett. 22, 93-100.

Ferenczy A. (1977). Anatomy and histology of the cervix. In: Pathology of the female genital tract. Blaustein, A. (eds). Springer. New York, NY. pp 102-123.

Ferenczy A. and Wright T.C. (2013). Anatomy and histology of the cervix. In: Blaustein's pathology of the female genital tract. Kurman R.J. (eds). Springer. New York, N. pp 185-201.

Fernandez C.D., Porto E.M., Arena A.C. and Kempinas W.D. (2008). Effects of altered epididymal sperm transit time on sperm quality. Int. J. Androl. 31, 427-437.

França L.R., Auharek S.A., Hess R.A., Dufour J.M. and Hinton B.T. (2012). Blood-tissue barriers: morphofunctional and immunological aspects of the blood-testis and blood-epididymal barriers. Adv. Exp. Med. Biol. 763, 237-259.

Gatimel N., Moreau J., Parinaud J. and Léandri R.D. (2017). Sperm morphology: assessment, pathophysiology, clinical relevance, and state of the art in 2017. Andrology 5, 845-862.

Ghio A.J. and Roggli V.L. (2021). Perls' Prussian blue stains of lung tissue, bronchoalveolar lavage, and sputum. J. Environ. Pathol. Toxicol. Oncol. 40, 1-15.

Goacher E., Randell R., Williams B and Treanor D. (2017). The diagnostic concordance of whole slide imaging and light microscopy: a systematic review. Arch. Pathol. Lab. Med. 141, 151-161.

Gundersen H.J., Bendtsen T.F., Korbo L., Marcussen N., Moller A., Nielsen K., Nyengaard J.R., Pakkenberg B., Sorensen F.B., Vesterby A. and West M.J. (1988a). Some new, simple and efficient stereological methods and their use in pathological research and diagnosis. APMIS 96, 379-394.

Gundersen H.J., Bagger P., Bendtsen T.F., Evans S.M., Korbo L., Marcussen N., Moller A., Nielsen K., Nyengaard J.R., Pakkenberg B., Sorensen F.B., Vesterby A. and West M.J. (1988b). The new stereological tools: disector, fractionator, nucleator and point sampled intercepts and their use in pathological research and diagnosis. APMIS 96, 857-881.

Guven S., Muci E. and Unsal M.A. (2010). The effects of carbon dioxide pneumoperitoneum on ovarian blood flow, oxidative stress markers, and morphology during laparoscopy: a rabbit model. Fertil. Steril. 93, 1327-1332.

Hamed M.A., Ekundina V.O. and Akhigbe R.E. (2023). Psychoactive drugs and male fertility: impacts and mechanisms. Reprod. Biol. Endocrinol. 21, 69.

He W., Liu H., Hu L., Wang Y., Huang L., Liang A., Wang X., Zhang Q., Chen Y., Li S., Wang J. and Lei X. (2021). Icariin improves testicular dysfunction via enhancing proliferation and inhibiting mitochondria-dependent apoptosis pathway in high-fat diet and streptozotocin-induced diabetic rats. Reprod. Biol. Endocrinol. 19, 168.

Howard V. and Reed M. (2004). Unbiased stereology: three-dimensional measurement in microscopy. Garland Science.

Ige S.F., Olaleye S.B., Akhigbe R.E., Akanbi T.A., Oyekunle O.A. and Udoh U.S. (2012a). Testicular toxicity and sperm quality following cadmium exposure in rats: Ameliorative potentials of Allium cepa. J. Hum. Reprod. Sci. 5, 37-42.

Ige S.F. and Akhigbe R.E. (2012b). The role of *Allium cepa* on aluminum-induced reproductive dysfunction in experimental male rat models. J. Hum. Reprod. Sci. 5, 200-205.

Jia S. and Zhao F. (2022). Ex vivo development of the entire mouse fetal reproductive tract by using microdissection and membrane-based organ culture techniques. Differentiation 123, 42-49.

Johnsen S.G. (1970). Testicular biopsy score count--a method for registration of spermatogenesis in human testes: normal values and results in 335 hypogonadal males. Hormones 1, 2-25.

Kaufman M. (2010). Development of the murine reproductive system. GUDMAP Consortium. Available at https://www.gudmap.org/tutorials/urogenital-dev/reproductive-system/

Kerr J.B., Abbenhuys D.C. and Irby D.C. (1986). Crystalloid formation in Leydig cells of rats (*Rattus fuscipes*). An ultrastructural and hormonal study. Cell. Tissue Res. 245, 91-100.

Khati W.H. and Hammouche S. (2021). Histomorphometrical study of the testis in the desert Rodent, *Gerbillus tarabuli*, sexually immature and adult during the annual reproductive cycle. Anat. Histol. Embryol. 50, 324-332.

Khati W.H., Moudilou E.N., Exbrayat J.M. and Hammouche S. (2018). Immunolocalization of RFamide-related peptide 3 in a desert rodent Gerbillus tarabuli during seminiferous epithelium cycle. Tissue Cell 55, 1-2.

Khati W.H., Al Mutery A.F., Ricken A. and Akhigbe R.E. (2022). Progress in research on the reproductive function in the sand rat (*Psammomys obesus*): A review. Gen. Comp. Endocrinol. 331, 114161.

Levine H., Jørgensen N., Martino-Andrade A., Mendiola J., Weksler-Derri D. and Mindlis I. (2017). Temporal trends in sperm count: a systematic review and meta-regression analysis. Hum. Reprod. Update 23, 646-659.

Lie G. and Hutson J.M. (2011). The role of cremaster muscle in testicular descent in humans and animal models. Pediatr. Surg. Int. 27, 1255-1265.

Maree L., Du Plessis S.S., Menkveld R. and Van der Horst G. (2010). Morphometric dimensions of the human sperm head depend on the staining method used. Hum. Reprod. 25, 1369-1382.

Martelli A., Russo V., Mauro A., Di Giacinto O., Nardinocchi D. and Mattioli M. (2017). insights into ovarian follicle angiogenesis: Morphological and chronological vascular remodeling from primordial to ovulating follicles. SM Vasc. Med. 2, 1009.

Mathias F.T., Romano R.M., Kizys M.M., Kasamatsu T., Giannocco G., Chiamolera M.I., Dias-da-Silva M.R. and Romano M.A. (2015). Daily exposure to silver nanoparticles during prepubertal development decreases adult sperm and reproductive parameters. Nanotoxicology 9, 64-70.

Mattfeldt T., Mall G., Gharehbaghi H. and Möller P. (1990). Estimation of surface area and length with the orientator. J. Microsc. 159, 301-317.

Merkwitz C., Blaschuk O., Eplinius F., Winkler J., Prömel S., Schulz A. and Ricken A. (2016a). A simple method for inducing estrous cycle stage-specific morphological changes in the vaginal epithelium of

immature female mice. Lab. Anim. 50, 344-353.
Merkwitz C., Blaschuk O., Schulz A. and Ricken A.M. (2016b). Comments on methods to suppress endogenous β-Galactosidase activity in mouse tissues expressing the LacZ reporter gene. J. Histochem. Cytochem. 64, 579-586.
Montoto L.G., Arregui L., Sánchez N.M., Gomendio M. and Roldan E.R. (2012). Postnatal testicular development in mouse species with different levels of sperm competition. Reproduction 143, 333-346.
Morales C., García-Pardo L., Reymundo C., Bellido C., Sánchez-Criado J.E. and Gaytán F. (2000). Different patterns of structural luteolysis in the human corpus luteum of menstruation. Hum. Reprod. 15, 2119-2128.
Morawietz G., Ruehl-Fehlert C., Kittel B., Bube A., Keane K., Halm S., Heuser A and Hellmann J. (2004). Revised guides for organ sampling and trimming in rats and mice--part 3: A joint publication of the RITA) and NACAD) Groups. Exp. Toxicol. Pathol. 55, 433-449.
Mruk D.D. and Cheng C.Y. (2015). The mammalian blood-testis barrier: Its biology and regulation. Endocr. Rev. 36, 564-591.
Mu Y., Yan W., Yin T., Zhang Y., Li J. and Yang J. (2017). Diet-induced obesity impairs spermatogenesis: a potential role for autophagy. Sci. Rep. 7, 43475.
Noorafshan A., Ahmadi M. and Mesbah S.F. (2013). Stereological study of the effects of letrozole and estradiol valerate treatment on the ovary of rats. Clin. Exp. Reprod. Med. 40, 115-121.
Nussey S.S. and Whitehead S.A. (2001). The gonad. In: Endocrinology: an integrated approach. BIOS Scientific Publishers. Oxford.
Ogedengbe O.O., Naidu E.C., Akang E.N., Offor U., Onanuga I.O., Peter A.I., Jegede A.I. and Azu O.O. (2018). Virgin coconut oil extract mitigates testicular-induced toxicity of alcohol use in antiretroviral therapy. Andrology 6, 616-626.
Ogundola A.F., Akhigbe R.E., Saka W.A., Adeniyi A.O., Adeshina O.S., Babalola D.O. and Akhigbe T.M. (2021). Contraceptive potential of Andrographis paniculata is via androgen suppression and not induction of oxidative stress in male Wistar rats. Tissue Cell 73, 101632.
Ombelet W., Menkveld R., Kruger T.F. and Steeno O. (1995). Sperm morphology assessment: historical review in relation to fertility. Hum. Reprod. Update 1, 543-557.
Oyedokun P.A., Akhigbe R.E., Ajayi L.O. and Ajayi A.F. (2023). Impact of hypoxia on male reproductive functions. Mol. Cell. Biochem. 478, 875-885.
Patil H.A., Patil A. and Mahajan S.V. (2015). Histopathological findings in uterus and cervix of hysterectomy specimens. MVP J. Med. Sci. 26-29.
Pelletier R.M. (2011). The blood-testis barrier: the junctional permeability, the proteins and the lipids. Prog. Histochem. Cytochem. 46, 49-127.
Perrard M.H., Sereni N., Schluth-Bolard C., Blondet A., d′ Estaing S.G., Plotton I., Morel-Journel N., Lejeune H., David L. and Durand P. (2016). Complete human and rat ex vivo spermatogenesis from fresh or frozen testicular tissue. Biol. Reprod. 95, 89.
Planinić A., Marić T., Bojanac A.K. and Ježek D. (2022). Reinke crystals: Hallmarks of adult Leydig cells in humans. Andrology 10, 1107-1120.
Pop O.T., Cotoi C.G., Plesea I.E., Gherghiceanu M., Enache S.D., Mandache E., Hortopan G. and Plesea R.M. (2011). Histological and ultrastructural analysis of the seminiferous tubule wall in ageing testis. Rom. J. Morphol. Embryol. 52, 241-248.
Puchtler H. and Waldrop F.S. (1979). On the mechanism of Verhoeff's elastica stain: a convenient stain for myelin sheaths. Histochemistry 62, 233-247.
Rendi M.H., Muehlenbachs A., Garcia R.L. and Boyd K.L. (2012). Female reproductive system. In: Comparative anatomy and histology. Treuting P.M. and Dintzis S.M. (eds). Academic Press. pp 253-284.
Robb G., Amann R. and Killian G. (1978). Daily sperm production and epididymal sperm reserves of pubertal and adult rats. J. Reprod. Fertil. 54, 103-107.
Sato J., Hashimoto S., Doi T., Yamada N. and Tsuchitani M. (2014). Histological characteristics of the regression of corpora lutea in wistar hannover rats: the comparisons with sprague-dawley rats. J. Toxicol. Pathol. 27, 107-113.
Scherle W. (1970). A simple method for volumetry of organs in quantitative stereology. Mikroskopie 26, 57-60.
Segal T.R. and Giudice L.C. (2022). Systematic review of climate change effects on reproductive health. Fertil. Steril. 118, 215-223.
Sheehan D.C. and Hrapchak B.B. (1973). Theory and practice of histotechnology. St-Louis. C.V. Mosby.
Shokri S., Hemadi M. and Aitken R.J. (2012). Transmission electron microscopy for the quantitative analysis of testis ultrastructure. Chapter 7. INTECH Open Access Publisher, USA. pp 113-126.
Siu M.K. and Cheng C.Y. (2004). Extracellular matrix: recent advances on its role in junction dynamics in the seminiferous epithelium during spermatogenesis. Biol. Reprod. 71, 375-391.
Slaoui M. and Fiette L. (2011). Histopathology procedures: from tissue sampling to histopathological evaluation. Methods Mol. Biol. 691, 69-82.
Slaoui M., Bauchet A.L and Fiette L. (2017). Tissue sampling and processing for histopathology evaluation. Methods Mol. Biol. 1641, 101-114.
Soukup A. and Tylová E. (2014). Essential methods of plant sample preparation for light microscopy. Methods Mol. Biol. 1080, 1-23.
Stasolla C and Yeung E.C. (2015). Paraffin and polyester waxes. Plant Microtechniques and Protocols. pp. 45-66.
Stewart C.A., Fisher S.J., Wang Y., Stewart M.D., Hewitt S.C., Rodriguez K.F., Korach K.S., and Behringer R.R. (2011). Uterine gland formation in mice is a continuous process, requiring the ovary after puberty, but not after parturition. Biol. Reprod. 85, 954-964.
Suarez S.S. (2002). Gamete transport. In: Fertilization. Academic Press, 3-28.
Tijani K.H., Oyende B.O., Awosanya G.O., Ojewola R.W. and Yusuf A.O. (2014). Assessment of testicular volume: A comparison of fertile and sub-fertile West African men. African J. Urol. 20, 136-140.
Tremellen K. (2008). Oxidative stress and male infertility--a clinical perspective. Hum. Reprod. Update 14, 243-258.
Tuominen V.J., Ruotoistenmäki S., Viitanen A., Jumppanen M. and Isola J. (2010). ImmunoRatio: a publicly available web application for quantitative image analysis of estrogen receptor (ER), progesterone receptor (PR), and Ki-67. Breast Cancer Res. 12, R56.
Vu Z., Gonzalez G., Stewart C.A., Mehra S. and Behringer R.R. (2018). Volumetric imaging of the developing prepubertal mouse uterine epithelium using light sheet microscopy. Mol. Reprod. Dev. 85, 397-405.
Wei S.M., Yan Z.Z. and Zhou J. (2009). Curcumin attenuates ischemia-reperfusion injury in rat testis. Fertil. Steril. 91, 271-277.
World Health Organization (2021). WHO laboratory manual for the examination and processing of human semen 6th ed. WHO Press.

Geneva, Switzerland.
Yigiter M., Halici Z., Odabasoglu F., Keles O.N., Atalay F., Unal B. and Salman A.B. (2011). Growth hormone reduces tissue damage in rat ovaries subjected to torsion and detorsion: biochemical and histopathologic evaluation. Eur. J. Obstet. Gynecol. Reprod. Biol. 157, 94-100.
Zamani A., Saki F., Hatami N. and Koohpeyma F. (2020). Stereological assessment of the effects of vitamin D deficiency on the rat testis. BMC Endocr. Disord. 20, 1-8.
Zare S., Hossein Dabbaghmanesh M., Noorafshan A., Koohpeyma F., Bakhshayeshkaram M. and Montazeri-Najafabady N. (2019). Protective effect of vitamin E and vitamin C alone and in combination on testicular damage induced by sodium metabisulphite in rats: a stereological study. Andrologia 51, e13193.
Zirkin B.R. and Goldberg E. (2018). Spermatids. Encyclipedia of reproduction. Second Edition. Elsevier Press. pp 42-46.

Accepted December 1, 2023